

# Subaru weak-lensing measurement of a $z = 0.81$ cluster discovered by the Atacama Cosmology Telescope Survey

Hironao Miyatake<sup>1,2,3</sup>, Atsushi J. Nishizawa<sup>2</sup>, Masahiro Takada<sup>2</sup>, Rachel Mandelbaum<sup>3,4</sup>, Sogo Mineo<sup>1,2</sup>, Hiroaki Aihara<sup>1,2</sup>, David N. Spergel<sup>2,3</sup>, Steven J. Bickerton<sup>2,3</sup>, J. Richard Bond<sup>5</sup>, Amir Hajian<sup>5</sup>, Matt Hilton<sup>6,7</sup>, Adam D. Hincks<sup>5</sup>, John P. Hughes<sup>8</sup>, Leopoldo Infante<sup>9</sup>, Yen-Ting Lin<sup>10</sup>, Robert H. Lupton<sup>3</sup>, Tobias A. Marriage<sup>11</sup>, Danica Marsden<sup>12</sup>, Felipe Menanteau<sup>8</sup>, Satoshi Miyazaki<sup>13</sup>, Kavilan Moodley<sup>7</sup>, Michael D. Niemack<sup>14</sup>, Masamune Oguri<sup>2</sup>, Paul A. Price<sup>3</sup>, Erik D. Reese<sup>15</sup>, Cristóbal Sifón<sup>9,16</sup>, Edward J. Wollack<sup>17</sup>, Naoki Yasuda<sup>2</sup>

<sup>1</sup> Department of Physics, The University of Tokyo, Bunkyo, Tokyo 113-0031, Japan

<sup>2</sup> Kavli Institute for the Physics and Mathematics of the Universe (Kavli IPMU, WPI), The University of Tokyo, Kashiwa, Chiba 277-8582, Japan

<sup>3</sup> Department of Astrophysical Sciences, Princeton University, Princeton, NJ 08544, USA

<sup>4</sup> Department of Physics, Carnegie Mellon University, Pittsburgh, PA 15213, USA

<sup>5</sup> Canadian Institute for Theoretical Astrophysics, University of Toronto, Toronto, ON M5S 3H8, Canada

<sup>6</sup> School of Physics and Astronomy, University of Nottingham, University Park, Nottingham, NG7 2RD, UK

<sup>7</sup> Astrophysics & Cosmology Research Unit, School of Mathematics, Statistics & Computer Science, University of KwaZulu-Natal, Durban 4041, South Africa

<sup>8</sup> Department of Physics and Astronomy, Rutgers, The State University of New Jersey, Piscataway, NJ 08854, USA

<sup>9</sup> Departamento de Astronomía y Astrofísica, Facultad de Física, Pontificia Universidad Católica de Chile, Casilla 306, Santiago 22, Chile

<sup>10</sup> Institute of Astronomy and Astrophysics, Academia Sinica, Taipei, Taiwan

<sup>11</sup> Department of Physics and Astronomy, The Johns Hopkins University, Baltimore, MD 21218, USA

<sup>12</sup> Department of Physics, University of California, Santa Barbara, CA 93106, USA

<sup>13</sup> National Astronomical Observatory of Japan, Mitaka, Tokyo 181-8588, Japan

<sup>14</sup> NIST Quantum Devices Group, Boulder, CO 80305, USA

<sup>15</sup> Department of Physics and Astronomy, University of Pennsylvania, 209 South 33rd Street, Philadelphia, PA 19104, USA

<sup>16</sup> Leiden Observatory, Leiden University, NL-2300 RA Leiden, Netherlands

<sup>17</sup> NASA/Goddard Space Flight Center, Greenbelt, MD 20771, USA

13 June 2021

## ABSTRACT

We present a Subaru weak lensing measurement of ACT-CL J0022.2–0036, one of the most luminous, high-redshift ( $z = 0.81$ ) Sunyaev-Zel’dovich (SZ) clusters discovered in the 268 deg<sup>2</sup> equatorial region survey of the Atacama Cosmology Telescope that overlaps with SDSS Stripe 82 field. Ours is the first weak lensing study with Subaru at such high redshifts. For the weak lensing analysis using  $i'$ -band images, we use a model-fitting (Gauss-Laguerre shapelet) method to measure shapes of galaxy images, where we fit galaxy images in different exposures simultaneously to obtain best-fit ellipticities taking into account the different PSFs in each exposure. We also take into account the astrometric distortion effect on galaxy images by performing the model fitting in the world coordinate system. To select background galaxies behind the cluster at  $z = 0.81$ , we use photometric redshift (photo- $z$ ) estimates for every galaxy derived from the co-added images of multi-passband  $Br'i'z'Y$ , with PSF matching/homogenization. After a photo- $z$  cut for background galaxy selection, we detect the tangential weak lensing distortion signal with a total signal-to-noise ratio of about 3.7. By fitting a Navarro-Frenk-White model to the measured shear profile, we find the cluster mass to be  $M_{200\bar{\rho}_m} = [7.5^{+3.2}_{-2.8}(\text{stat.})^{+1.3}_{-0.6}(\text{sys.})] \times 10^{14} M_{\odot}/h$ . The weak lensing-derived mass is consistent with previous mass estimates based on the SZ observation, with assumptions of hydrostatic equilibrium and virial theorem, as well as with scaling relations between SZ signal and mass derived from weak lensing, X-ray, and velocity dispersion, within the measurement errors. We also show that the existence of ACT-CL J0022.2–0036 at  $z = 0.81$  is consistent with the cluster abundance prediction of the  $\Lambda$ -dominated cold dark matter structure formation model. We thus demonstrate the capability of Subaru-type ground-based images for studying weak lensing of high-redshift clusters.

**Key words:** cosmology: observation — gravitational lensing — galaxy clusters — cosmic microwave background

## 1 INTRODUCTION

Clusters of galaxies are the most massive gravitationally-bound objects in the Universe, and therefore are very sensitive to cosmological parameters, including the dark energy equation of state (Kitayama & Suto 1997; Vikhlinin et al. 2009, and references therein). The growth of cosmic structures in the Universe is regulated by a competition between gravitational attraction and cosmic expansion. Hence, if the evolution of the cluster mass function can be measured robustly, the influence of dark energy on the growth of structure, and thus the nature of dark energy, can be extracted. Furthermore, since dark matter plays an essential role in the formation and evolution of clusters, the mass distribution in cluster regions contains a wealth of information on the nature of dark matter (e.g., Broadhurst et al. 2005; Okabe et al. 2010; Oguri et al. 2012).

The Sunyaev-Zel'dovich (SZ) effect, in which photons of the cosmic microwave background (CMB) scatter off electrons of the hot intracluster medium, is a powerful way of finding massive clusters, especially at high redshift (Zeldovich & Sunyaev 1969; Sunyaev & Zeldovich 1972; also see Carlstrom et al. 2002 for a thorough review), for several reasons. First, the SZ effect has a unique frequency dependence: below 218GHz, it appears as a decrement (or cold spot) in the CMB temperature map, while at higher frequencies it appears as an increment (hot spot). Second, unlike optical and X-ray observations, the SZ effect does not suffer from the cosmological surface brightness-dimming effect; thus, it is independent of redshift, offering a unique way of detecting all clusters above some mass limit irrespective of their redshifts. Currently there are several ongoing arcminute-resolution, high-sensitivity CMB experiments, such as the Atacama Cosmology Telescope (ACT; Swetz et al. 2011) and the South Pole Telescope (SPT; Carlstrom et al. 2011). These SZ surveys are demonstrating the power of SZ surveys for finding clusters (Marriage et al. 2011), and have already shown that the SZ-detected clusters can be used to constrain cosmology (Vanderlinde et al. 2010; Sehgal et al. 2011; Reichardt et al. 2012).

However, the SZ effect itself does not necessarily provide robust mass estimates of high-redshift clusters, because of several assumptions that may not be valid, such as dynamical and hydrostatic equilibrium, or the cluster mass-scaling relation inferred from low-redshift clusters. The relationship between cluster observables and mass is of critical importance for cluster-based cosmology, so it is critical to establish a well-calibrated scaling relation in order to robustly use SZ-detected clusters for cosmology. Gravitational weak lensing (WL), the shape distortion of background galaxies due to the mass in clusters, is a well-known tool for unveiling the distribution of matter in clusters, regardless of the dynamical state (see Bartelmann & Schneider 2001, for a thorough review). WL can therefore calibrate the relation between SZ observables and mass, and ultimately constrain cosmology with SZ-selected clusters.

Thus there is a strong synergy between optical (including WL) and SZ surveys. First, optical surveys enable a comparison between SZ and WL signals and optical richness for the SZ-detected clusters. Second, a multi-band optical imaging survey can reveal (photometric) redshifts for SZ-detected clusters. For these reasons, there are joint experiments being planned: the Subaru Hyper Suprime-Cam (HSC) survey (Miyazaki et al. 2006)<sup>1</sup> combined with the ACT

survey, and the Dark Energy Survey (DES; The Dark Energy Survey Collaboration 2005)<sup>2</sup> with the SPT survey.

With these upcoming SZ-WL surveys in mind, in this paper, we study WL signal of a SZ-detected cluster, ACT-CL J0022.2–0036 (hereafter ACTJ0022) at  $z = 0.81$ , using multi-passband data with the current Subaru prime-focus camera, Suprime-Cam (Miyazaki et al. 2002b). Subaru Suprime-Cam is one of the best available ground-based instruments to carry out accurate WL measurements, thanks to the excellent image quality (median seeing FWHM is 0.6–0.7'') and wide field-of-view,  $\sim 0.25 \text{ deg}^2$  (Miyazaki et al. 2002a; Broadhurst et al. 2005; Okabe et al. 2010; Oguri et al. 2012). ACTJ0022 is one of the most luminous SZ clusters discovered in the 148-GHz ACT map of 268 square degrees, which is a part of 500 square degrees in its equatorial survey field taken in 2009 and 2010 (Reese et al. 2012; Hasselfield in prep.) and overlaps with SDSS Stripe 82 field. Long-slit follow-up spectroscopy at the Apache Point Observatory of the brightest cluster galaxy (BCG) confirms the redshift of  $z = 0.81$  (Menanteau in prep.). To do the WL analysis, we analyze different exposures simultaneously to model the shape of every galaxy, based on the elliptical Gauss-Laguerre (EGL) shapelet method (Bernstein & Jarvis 2002; Nakajima & Bernstein 2007). In the multi-exposure fitting, we can keep the separate PSF of each exposure, and therefore keep the highest-resolution PSF in the analysis, which is not the case for the use of stacked images for the WL analysis. Furthermore, we use photometric redshift (photo- $z$ ) information, derived from the stacked images of Subaru  $Br'i'z'Y$  data, in order to define a secure sample of background (therefore lensed) galaxies. Thus, we combine shape measurements and photo- $z$  information to study the mass of ACTJ0022, which has not been fully explored in previous WL studies of high-redshift clusters. Our study assesses the capability of ground-based data for a WL study of high-redshift, SZ-detected clusters. We also discuss the implications of our WL result for the SZ-cluster mass scaling relations, and whether or not the estimated mass of ACTJ0022 is consistent with the  $\Lambda$ CDM structure formation model that is constrained by various cosmological data sets, using the method in Mortonson et al. (2011).

This paper is organized as follows. In Section 2, we describe the Subaru/Suprime-Cam follow-up observations. In Section 3, we describe the data analysis including data reduction, photo- $z$  estimation, and galaxy shape measurement. Then we show the WL result for ACTJ0022, and discuss the systematic error issues and the cosmological implication in Section 4. Throughout this paper we use the AB magnitude system. Unless explicitly stated, we adopt a flat  $\Lambda$ CDM cosmology with  $\Omega_m = 0.27$  and  $H_0 = 72 \text{ km s}^{-1} \text{ Mpc}^{-1}$ .

## 2 OBSERVATION

We observed the ACTJ0022 field on December 4th, 2010, using Suprime-Cam (Miyazaki et al. 2002b) with five broadband filters ( $Br'i'z'Y$ ) on the Subaru Telescope (Iye et al. 2004), as summarized in Table 1. The RGB image of the cluster is shown in Fig. 1. All passbands are used for photo- $z$ , whereas only the  $i'$ -band image is used for shape measurement. The choice of filters and depths was determined by using a mock catalog of galaxies based on the methods of Nishizawa et al. (2010). We constructed the mock catalog based on the COSMOS photometric catalog (Ilbert et al. 2009), and used the catalog to estimate the required accuracy of photometric

<sup>1</sup> <http://www.naoj.org/Projects/HSC/index.html>; also see <http://sumire.ipmu.jp/>

<sup>2</sup> <http://www.darkenergysurvey.org/>

redshifts, available from the multi-color data, in order to minimize contamination of foreground and cluster-member galaxies (therefore unlensed galaxies) to the lensing analysis.

### 3 DATA ANALYSIS

#### 3.1 Analysis Overview

Figure 2 shows a flow chart of our data analysis procedure. In this analysis, we have used the HSC pipeline for the tasks shown as shaded blocks. The HSC pipeline is now actively being developed for analysis of the HSC survey data, based on the data reduction pipeline developed for LSST. Due to the large data volume (HSC will provide  $\sim 2.3$ GB per exposure), the pipeline aims to reduce the data in an automated way from raw data to catalogs. Core parts of the pipeline are written in C++ to enhance computing speed, then are wrapped by a Python layer used to script together the core steps of the analysis. We emphasize that our study is the first case where the HSC pipeline is used for science. The version of the pipeline we use is HSC.17.

The raw chip data first undergoes chip-based data reduction. At this stage, instrumental signatures such as bias, overscan, and flat are removed, and the PSF is determined (see Section 3.2 for details). The corrected chip data and PSF are passed to two branches, for redshift determination and shape measurement of each galaxy. To estimate photo- $z$ , we stack all exposures for each chip, match PSFs between different passbands, detect objects, carry out photometry, and finally feed the measured magnitudes into the photo- $z$  software (see details in Section 3.3).

For the shape measurement, we employ the EGL method that aims to extract shape information by representing the PSF and galaxy image with orthogonal basis functions (Bernstein & Jarvis 2002; Nakajima & Bernstein 2007). We analyze individual exposures simultaneously, which enables us to avoid mixing PSFs taken in different epochs and interpolating pixel values. Details of the shape measurement will be described in Section 3.4. Finally, the photo- $z$  and shapes are used for cluster mass estimation (Section 4).

#### 3.2 Chip-based Data Reduction

For each chip, the HSC pipeline produces three image planes with the same dimensions (approximately  $2k \times 4k$  pixels). The first is an image plane that contains the corrected image data. The second is a variance plane that stores theoretical variance of each pixel; the noise is first estimated from the raw image by assuming Poisson noise of photon counts in each pixel, and then the noise is properly propagated at each stage of the reduction. The third is a mask plane that has a 16-bit integer for each pixel. Different bits are used for different masks to indicate saturation and other issues.

##### 3.2.1 Instrumental Signature Removal

First, pixels having a value greater than a saturation threshold are masked as SAT. Different saturation thresholds are set for each CCD according to its own characteristics.

A CCD has four outputs (or amps), each of which reads out  $4177 \times 512$  pixels. Thus the raw data of each CCD has four stripes of image data, between which overscan regions are laid out. Using the median of the overscan regions, the bias level is subtracted. The overscan regions are then trimmed and the four stripes are combined.

Now that we have signals only from photons, the variance plane is created. Assuming Poisson statistics, the variance at pixel  $(x, y)$  is calculated as  $\text{Var}(x, y) = I(x, y)/g$ , where  $I(x, y)$  is the pixel count in ADU and  $g$  is the gain (the number of electrons per ADU). Note that we use gains known for each amplifier independently.

Flat fielding and fringe correction are carried out using the dome flat and sky frames, respectively. The CCD defects known beforehand are masked as BAD. We also masked the pixels surrounding the saturation masks by two additional pixels to avoid effects of electrons leaking out from the saturated pixels.

We performed initial sky subtraction as follows (we refined the sky subtraction at a later stage as we will describe below). A chip image is divided into patches, each of which contains  $1024 \times 1024$  pixels, and the background in each patch is calculated using the  $3\text{-}\sigma$  clipping mean method. The background field is then obtained by spline-interpolating the measured mean values at the center of each patch. We then subtracted the background level in each pixel from the image.

##### 3.2.2 Calibration

We use bright sources to perform PSF measurement and astrometry.

First, we need to remove cosmic rays from the images. Assuming a Gaussian PSF with FWHM  $1.0''$  as an initial guess, we regard objects having sharper jump in the flux in one dimension and smaller size than the PSF as a cosmic ray, and mask the associated pixels as CR.

We perform detection of bright objects as follows. By convolving the image with the Gaussian PSF of  $1.0''$  FWHM, we register a set of connected pixels above the threshold value  $n_{\text{th}}\sigma$  as a footprint of an object, where  $\sigma$  is the sky noise and we employed  $n_{\text{th}} = 2$  in this analysis. Then we define bright objects as a subset of objects with peak value above  $n_{\text{th,ex}} \times n_{\text{th}}\sigma$  in the original image, where we employed  $n_{\text{th,ex}} = 5$  (i.e. we adopted  $10\sigma$  for the peak value). At this step, we again perform sky subtraction by using finer-size patches, each of which has  $128 \times 128$  pixels, but masking the footprint of detected objects. For the sky subtraction, we noticed that it is important to mask outskirts of the detected objects; otherwise, the sky is over-subtracted. This is the main reason we employed a rather conservative value of  $n_{\text{th}} = 2$  for the threshold value of object detection.

Then we measured the PSF flux and second-order moments of each bright object, using its image in the footprint. The PSF flux  $f_{\text{PSF}}$  is defined by minimizing  $\chi^2 = \sum_{\alpha}^{N_{\text{pix}}} [I_{\text{data}}(\mathbf{x}_{\alpha}) - f_{\text{PSF}} \hat{I}_{\text{PSF}}(\mathbf{x}_{\alpha})]^2 / \sigma_{\alpha}^2$ , where the index  $\alpha$  runs over the pixels of the footprint,  $I_{\text{data}}(\mathbf{x}_{\alpha})$  is the image value at the  $\alpha$ -th pixel,  $\sigma_{\alpha}$  is the noise at the pixel,  $\hat{I}_{\text{PSF}}$  is the PSF function (the Gaussian function of  $1.0''$  FWHM up to this stage), and  $f_{\text{PSF}}$  is a model parameter for the PSF flux. Note that the PSF profile  $\hat{I}_{\text{PSF}}$  is normalized so as to satisfy  $\sum_{\alpha}^{N_{\text{pix}}} \hat{I}_{\text{model}}(\mathbf{x}_{\alpha}) = 1$ , and the center of the PSF profile  $\hat{I}_{\text{PSF}}$  is set to the object center. The best-fit  $f_{\text{PSF}}$  is obtained by minimizing the  $\chi^2$  above. This is a linear algebra problem, so  $f_{\text{PSF}}$  can be obtained without any ambiguity. We also estimate the second-order moments of the bright object, using adaptive moments defined as  $M_{ij} = \int W(\mathbf{x}) I(\mathbf{x}) x_i x_j d\mathbf{x}$ , where the integration runs over all the pixels in the footprint and  $W(\mathbf{x})$  is

filter	tot. exp. time [s]	# of exp.	frame ID	typ. seeing ["]	lim. mag.
<i>B</i>	600	3	1269250 - 1269279	0.66	25.9
<i>r'</i>	600	3	1269680 - 1269709	1.06	25.3
<i>i'</i>	2400	10	1269320 - 1269419	0.74	25.6
<i>z'</i>	3240	12	1269430 - 1269549	0.90	24.8
<i>Y</i>	3240	12	1269560 - 1269679	0.78	23.6

**Table 1.** Summary of the Subaru/Suprime-Cam observations. Note that the limiting magnitude is for  $3''$  aperture magnitude ( $5\sigma$ ). *Y*-band is a 1 micron filter with the red edge defined by the deep-depletion CCD response.

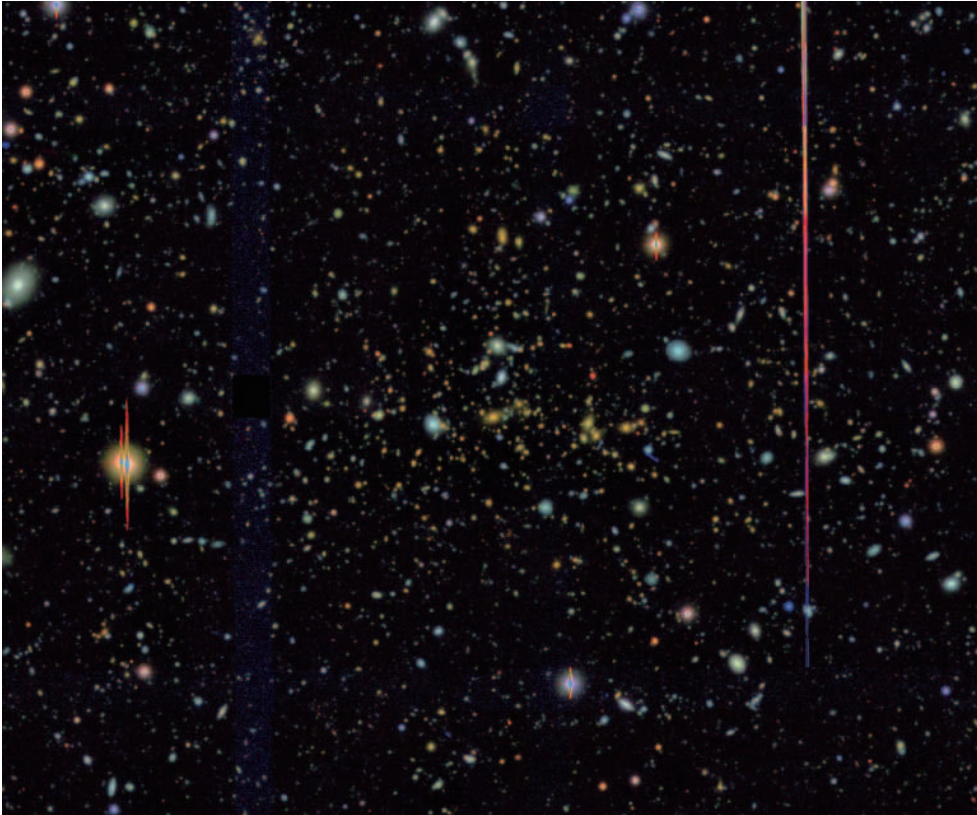


**Figure 1.** The Subaru/Suprime-Cam image of ACTJ0022, the region of about  $7 \times 9$  square arcminutes around the cluster center (its BCG position). North is up and west is right. The color image is made by combining the  $r'i'z'$  images. Note that an angular scale of  $1'$  corresponds to the transverse scale of  $322 \text{ kpc}/h$  at  $z = 0.81$ .

a weight function. We employed an elliptical Gaussian for  $W(\mathbf{x})$ , whose shape is matched to the object via an iterative procedure<sup>3</sup>.

### 3.2.3 PSF Determination

By using the PSF flux and the adaptive moments, we select star candidates for PSF determination as follows. We first remove objects having the PSF flux below  $f_{\text{lim}}$  in order to eliminate faint, small galaxies or low- $S/N$  stars. In this analysis, we employ  $f_{\text{min}} = 60000$  counts corresponding to apparent magnitude brighter than  $\simeq 21.8$  mag. We select star candidates from objects lying within the  $2\sigma$  regions around the peak in the two-dimensional distribution of  $I_{11}$  and  $I_{22}$ , because stars should have small moments and similar values. Since the variation of the second-order moments is

moderately large especially for the corner chip of the Suprime-Cam focal plane, we decided to employ the  $2\sigma$  threshold, rather than  $1\sigma$ , in order not to miss real stars in the selection. Note that with this large  $\sigma$  we can get compact galaxies, which will be rejected by the following process.

Next, using the star candidates on each CCD chip, the PSF is heuristically determined by principal component analysis (PCA; also known as Karhunen-Loève transform; Jolliffe 1986), with the algorithm from the SDSS imaging pipeline (Lupton et al. 2001). An image of each star candidate can be represented by linear combination of principal components (or eigenfunctions):

$$P(u, v) = \sum_{i=0}^{n_{\text{pc}}-1} a_i K_i(u, v), \quad (1)$$

where  $P(u, v)$  is the observed image,  $K_i(u, v)$  are the  $i$ -th principal components,  $n_{\text{pc}}$  is a parameter to determine up to which order principal component to include, and  $u, v$  is the pixel coord-

<sup>3</sup> [http://www.sdss3.org/dr8/algorithms/classify.php#photo\\_adapt](http://www.sdss3.org/dr8/algorithms/classify.php#photo_adapt)

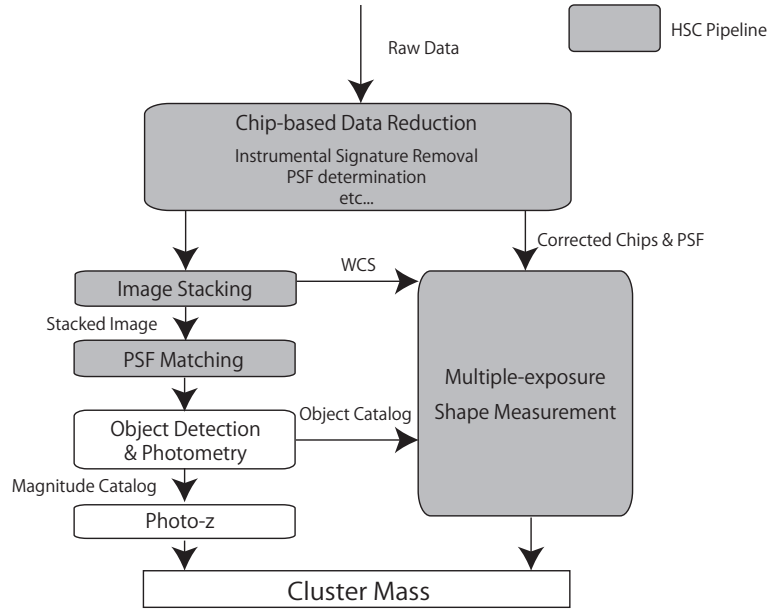


Figure 2. Flow chart of our data analysis procedures.

dinates relative to the origin of principal components. We include the spatial variation of PSF assuming that the spatial variation of the coefficients is modeled by the Chebyshev polynomials:

$$a_i \rightarrow a_i(x, y) \equiv \sum_{p+q \leq n_{sv}} c_{pq} T_p(x) T_q(y), \quad (2)$$

where  $x, y$  is the pixel coordinates of a given CCD chip,  $T_i(x)$  is the  $i$ -th Chebyshev polynomial (employed to prevent the polynomial from blowing up at the edge of chip),  $c_{pq}$  is the expansion coefficients, and  $n_{sv}$  is a parameter to determine which order of the polynomials to include in this interpolation. Note that the constraints to determine the coefficients  $c_{pq}$  are given at the positions of stars, used for PSF determination, and the coordinates  $(x, y)$  are normalized to  $[-1, 1]$  across the chip for our convenience. In this analysis, we set  $n_{pc}$  and  $n_{sv}$  to 6 and 4, respectively, which are decided after an iterative, careful study of the PSF determination (see Section 3.4.2 for details). The principal components  $K(u, v)$  and the coefficients  $a_i(x, y)$  enable us to reconstruct the PSF at arbitrary positions, which hereafter we refer to as the PCA PSF. Using the updated PSF estimate, the PSF flux is re-measured for each bright object in order to refine the star catalog (or remove the contaminating star-like objects). After several iterations, we use the refined PSF estimates for the update of cosmic ray masking and the following analysis.

### 3.2.4 Astrometry

The bright stars are matched to a reference catalog created from SDSS DR8 (Aihara et al. 2011) by using `astrometry.net`<sup>4</sup> (Lang et al. 2010), which is the *astrometry engine* to create astrometric meta-data for a given image. Based on the match list, we determine the world coordinate system (WCS) in the TAN-SIP convention (Shupe et al. 2005). For this chip-based astrometry, we used quadratic polynomials to obtain the transformation between

the celestial coordinates and pixel coordinates. The pixel scale of Subaru/Suprime-Cam is about  $0.2''$ , which in fact slightly changes with position due to the camera distortion. Note that we use the chip-based WCS when co-adding different exposures to make the stacked images, and then use the improved astrometry to renew the WCS for each chip.

### 3.3 Redshift Estimation

In this subsection, we describe the method for photometry, which will then be needed for photo- $z$  estimation of galaxies (the left branch of Fig. 2). Our method follows the prescription proposed by Hildebrandt et al. (2012). A brief summary of our method of determining galaxy photometry is: (1) stack (co-add) the corrected images of each passband for detection of fainter objects, (2) match the PSF across all the passband images, including PSF homogenization across spatial positions, and (3) measure the aperture photometry of each object, after the PSF matching, in order to robustly measure the colour of objects for the same *physical* region. Several photometry algorithms are now in development for the HSC pipeline. In this paper, we decided to use `SEXTRACTOR` (Bertin & Arnouts 1996) in order to follow the method of Hildebrandt et al. (2012). Below, we describe the details of this procedure.

#### 3.3.1 Stacking and PSF Matching/Homogenization

We stack different exposure images primarily by matching the positions of stars, which are used for astrometry as described in Section 3.2.4, but also by matching slightly fainter objects for a further improvement. The relative accuracy of our astrometry is  $\sim 0.03''$  (external + internal) and  $\sim 0.01''$  (internal only). Here, “external” means accuracy with respect to the external reference catalog and “internal” means accuracy within the exposures we analyse. For the stacked image, WCS based on the TAN-SIP convention is generated by using the matching list, where we used the polynomials including terms up to  $x^n y^m$ , where  $n + m = 10$  ( $x, y$  are the pixel coordinates from the center of the stacked image). We use the

<sup>4</sup> <http://astrometry.net/>

celestial coordinates for the multiple-exposure shape measurement as we will describe in Section 3.4.2. When co-adding the different images, we perform the scaling of each exposure based on the measured PSF in each chip, such that the PSF fluxes (or the fluxes of the same stars) in different exposures become identical. The scaling amplitude is typically within  $1 \pm 0.02$ . Using the WCS and scaling information, each exposure image is warped and the counts are scaled. The warping requires resampling (or interpolation) of pixel values for which we use the Lanczos3 algorithm to preserve independence of photon noise in between different pixels<sup>5</sup>. Note that the resampling for all the  $Br'i'z'Y$  images is matched to the  $i'$ -band WCS, the details of which will be described in Section 3.3.2. After these procedures, we stack all the exposures of a given passband.

To match PSFs of different passbands, we first find the largest PSF among the stacked  $Br'i'z'Y$  images. We run the PSF determination algorithm on each stacked image, and measure the adaptive moments of the PCA PSFs at several spatial positions across the image. The size of each PSF image is estimated from the adaptive moments as

$$\sigma = (M_{11}M_{22} - M_{12}^2)^{1/4} = |\det M|^{1/4}. \quad (3)$$

The largest PSF we found is  $\sim 2.6$  pixels, around the edge of the  $r'$ -band stacked image. For the PSF matching, we use the algorithm developed by Alard & Lupton (1998) and Alard (2000) (also see Huff et al. 2011, for the recent implementation). This method enables us to match the PSFs to an arbitrary, analytical PSF shape, the so-called target PSF, by convolving the observed image with the differential PSF kernel. The target PSF we use in this analysis is the Gaussian function, a convenient approximation to PSF, with  $\sigma = 2.6$  pixels matching the largest PSF above. Furthermore, we implement homogenization of the matched PSF across the spatial positions in the image; i.e., we use a spatially-varying kernel in order to have the same PSF across all the positions in the matched image.

Table 2 shows the size and ellipticity of PSFs before and after the PSF matching, where the error shows the standard deviation of the quantities across the field and the ellipticity is estimated from the adaptive moments as

$$(e_1, e_2) = \left( \frac{M_{11} - M_{22}}{M_{11} + M_{22}}, \frac{2M_{12}}{M_{11} + M_{22}} \right). \quad (4)$$

The PSF size in each band is matched to 2.6 pixels within about 1.5 per cent, and the ellipticity of the matched PSF is consistent with zero.

### 3.3.2 Photometry

We use SEXTRACTOR to perform object detection as well as photometry for the PSF-matched, stacked images. As we stressed, we want to measure the flux of each object for the *same* region (and with the *same* weight). First, we use the stacked  $i'$ -band image, before the PSF matching, for object detection as well as for defining the photometry region, because the images before the PSF matching are higher resolution and are less contaminated by the blending of neighboring objects. For the photometry region, in this analysis, we use the isophotal region around each object; we defined the

<sup>5</sup> The sinc function is the ideal interpolation, since it does not introduce any information whose frequency is higher than the pixel sampling scale. However, because of its infinite extent, we use a windowed approximation known as the Lanczos filter.

		$\sigma$ [pixel]	$e_1$	$e_2$
$B$	original	$1.39 \pm 0.04$	$0.055 \pm 0.023$	$-0.002 \pm 0.013$
	match	$2.61 \pm 0.02$	$-0.003 \pm 0.005$	$-0.001 \pm 0.004$
$r'$	original	$2.28 \pm 0.11$	$-0.032 \pm 0.018$	$-0.009 \pm 0.019$
	match	$2.57 \pm 0.06$	$-0.001 \pm 0.011$	$-0.002 \pm 0.012$
$i'$	original	$1.55 \pm 0.05$	$-0.019 \pm 0.025$	$-0.006 \pm 0.035$
	match	$2.61 \pm 0.03$	$0.001 \pm 0.008$	$-0.002 \pm 0.012$
$z'$	original	$1.91 \pm 0.06$	$-0.015 \pm 0.020$	$-0.022 \pm 0.026$
	match	$2.60 \pm 0.04$	$0.001 \pm 0.009$	$-0.003 \pm 0.013$
$Y$	original	$1.65 \pm 0.08$	$0.000 \pm 0.025$	$-0.023 \pm 0.035$
	match	$2.60 \pm 0.04$	$0.001 \pm 0.008$	$-0.002 \pm 0.012$

**Table 2.** The PSF size and average ellipticity for each passband stacked images. The row labelled as “original” or “match” shows the results for the stacked images with or without the PSF match/homogenization (see Section 3.3.1 for details).

group of connected pixels around each object, which have counts above 5 times the sky noise. We can obtain this group of pixels, called the *segmentation* region, using SEXTRACTOR; it is conceptually equivalent to the footprint in the HSC pipeline. Then we define the *same* photometry regions in the stacked  $Br'i'z'Y$  images by matching the segmentation region in the  $i'$ -band image to the other passband image via the WCS, as described in Section 3.3.1. After these procedures, we finally make the aperture magnitude MAG\_ISO, within the same segmentation region, for each object in each of the PSF-matched, stacked  $Br'i'z'Y$  images, using the dual mode of SEXTRACTOR, as suggested in Hildebrandt et al. (2012).

To determine the magnitude zero point, we identify the SDSS stars in the ACTJ0022 field and measure the star flux in a  $4.8''$  aperture on the PSF-matched images. We employ such a larger aperture in order to cover all the flux from stars smeared by the PSF matching. Although the SDSS DR8 photometry is calibrated at high precision (Aihara et al. 2011), we cannot directly compare the stellar fluxes inferred from the SDSS catalog with the measured fluxes of the Suprime-Cam data, because the  $r'i'z'$  filter responses are not exactly the same, and the  $B$ - and  $Y$ -passbands do not exist in the SDSS photometric system. Thus we need to infer the Suprime-Cam filter magnitudes for each star from the SDSS magnitudes using the following method. First, we fit the multi-band fluxes in  $ugriz$  for each stellar object in the SDSS catalog to a stellar atmosphere model from Castelli & Kurucz (2004). The model includes 3808 stellar spectra that are given as a function of various combinations of metallicities, effective temperatures, and surface gravity strengths. By convolving the best-fit spectrum with the response functions of the Suprime-Cam filters, we can estimate the Suprime-Cam filter magnitudes for each SDSS star. Note that the Suprime-Cam  $B$ -band magnitude is effectively interpolated between the SDSS passbands, whereas the  $Y$ -band magnitude is extrapolated from the SDSS magnitudes. Since the SDSS magnitudes are already calibrated for atmospheric extinction at a reference airmass of 1.3, we do not have to correct for the airmass difference between exposures. Using the above method, we determine the magnitude zero point of each band. The errors of the zero point are estimated from the scatters between the SDSS- and Suprime-Cam magnitudes as  $B$ : 0.048,  $r'$ : 0.090,  $i'$ : 0.043,  $z'$ : 0.080, and  $Y$ : 0.086 magnitudes.

We correct for Galactic dust extinction following the approach

in Schlegel et al. (1998) and the dust extinction map provided by the NASA/IPAC Infrared Science Archive<sup>6</sup>. The estimated extinctions ( $B: 0.098$ ,  $r': 0.066$ ,  $i': 0.050$ ,  $z': 0.036$ , and  $Y: 0.031$ ) are used to correct our photometry.

### 3.3.3 Photometric Redshift

For the photo- $z$  estimate, we use the publicly available code, *Le Phare*<sup>7</sup> (Arnouts et al. 1999; Ilbert et al. 2006), which is based on template-fitting of the galaxy spectral energy distribution (SED). The template set of SEDs that we use is based on the CWW (Coleman et al. 1980) and starburst templates (Kinney et al. 1996). The CWW templates were refined in order to better match the actual data from the CFHTLS as well as the VVDS spectroscopic data (Ilbert et al. 2006). In addition, *Le Phare* has a functionality to recalculate magnitude zero points so that the difference between the observed and model SEDs are adjusted using a training set of spectroscopic galaxies. In this analysis, we use spectroscopic galaxy catalogs from the SDSS DR8 (Aihara et al. 2011) and the Baryon Oscillation Spectroscopic Survey (BOSS; Eisenstein et al. 2011; Bolton et al. 2012; Dawson et al. 2012; Smee et al. 2012). For the ACTJ0022 field, we have 205 spectroscopic redshifts from the catalogs to use for the calibration. The offsets of the magnitude zero points obtained from this procedure are  $B: 0.072$ ,  $r': 0.057$ ,  $i': -0.023$ ,  $z': -0.053$ , and  $Y: 0.016$ , which are comparable to the zero point errors shown in Section 3.3.2.

As one validation of our photo- $z$ s, the left panel of Fig. 3 shows the photo- $z$  distribution for galaxies selected around the red sequence in the color-magnitude diagram, which are therefore likely to be cluster members. To be more precise, we employ the red sequence given by the ranges in  $19 < z' < 23$  and  $-0.12z' + 4.25 < r' - z' < -0.12z' + 4.75$ . In addition, we focus on the red galaxies located in a  $2000 \times 2000$  pixels region, or  $6.7 \times 6.7$  arcmin<sup>2</sup>, around the BCG (i.e. a proxy for cluster center), because a typical virial radius for a massive cluster is about 2 Mpc, which corresponds to about 1300 pixels at redshift  $z = 0.8$  for a  $\Lambda$ CDM model. After imposing these selection criteria, we find 238 red-sequence galaxies.

The figure compares our photo- $z$  estimates for the red galaxies with spectroscopically-selected member galaxies, which were taken using Gemini-south/GMOS (Program: GS-2011B-C-1, PI: F. Menanteau) as a part of the spectroscopic follow-up of ACT-SZ selected clusters (Sifón et al. 2012). Note that the Gemini spectroscopic galaxies shown here are all the member galaxies, within  $5000 \text{ km s}^{-1}$  with respect to the cluster. The distribution of photo- $z$  for these confirmed cluster member galaxies shows that there is a significant overlap of the photo- $z$ s with the spectroscopic redshifts around the cluster redshift  $z = 0.81$ . However, the figure also shows that there are some catastrophic failures of the photo- $z$ s around  $z_p \simeq 2.3$  and  $3.8$ . If we ignore these catastrophic photo- $z$  failures, the mean redshift of the photometric red-sequence galaxies is  $0.79 \pm 0.09$ , which is in good agreement with the cluster redshift within the error bars. In the following analysis, we conservatively use galaxies with photo- $z$ s  $0.95 < z_p < 2.0$  as the catalog of background galaxies. Thus we do not use the galaxies with  $z_p > 2$ , because the figure implies that the catalog can be contaminated by

unlensed member or foreground galaxies, which cause a dilution of the estimated lensing signals (e.g., Broadhurst et al. 2005).

The right panel of Fig. 3 shows the redshift distributions of photometric galaxies. The solid-line histogram is the photometric redshift distribution for galaxies that have  $S/N > 10$  for the  $3''$  aperture flux. The shaded histogram shows the redshift distribution for galaxies that are useful for weak lensing analysis; the galaxies have sufficiently large size and flux  $S/N$  for the shape measurement, as we will discuss in more detail in Section 3.4.1. Again, for the following lensing analysis, we use galaxies with  $0.95 < z_p < 2.0$  to minimize the contamination by photo- $z$  outliers.

## 3.4 Shape Measurement

For the shape measurement (the right branch of Fig. 2), we employ the EGL method which uses elliptical Gauss-Laguerre (GL) basis functions to model galaxy images. We also expand the method to simultaneous multiple-exposure measurement to avoid mixing different PSFs in different exposures as well as pixel resampling, which are systematic issues when using stacked images for the shape measurements.

### 3.4.1 Star-galaxy separation

As described in Section 3.3.2, we use the  $i'$ -band stacked image for object detection as well as for star-galaxy selection. Again note that we use the  $i'$ -band images for the shape measurement. We use the size-magnitude diagram to select stars from the locus of objects with nearly constant FWHM and  $19.5 < i' < 21.5$ , yielding about 650 stars in total, with mean size FWHM =  $0.69'' \pm 0.03''$ .

To select galaxies, we use objects that have FWHMs more than  $2\sigma$  above the stellar FWHM, where  $\sigma$  is the stellar size rms. At this stage, the number density is  $52.7 \text{ arcmin}^{-2}$ . We then applied the magnitude cut  $19 < i' < 25.6$ , where the faint end of the magnitude range is determined so that the total signal-to-noise ratio ( $S/N$ ) for the  $3''$  aperture flux should be greater than 5. The number density is reduced to  $48.6 \text{ arcmin}^{-2}$ . Together with the photo- $z$  cut (see Section 3.3.3), the resulting number density of source galaxies is about  $10.6 \text{ arcmin}^{-2}$ . Furthermore, after imposing size and  $S/N$  cuts for reliable shape measurements of galaxies, the final number density becomes  $3.2 \text{ arcmin}^{-2}$  (see Section 3.4.3 for details).

### 3.4.2 PSF fitting

First, we need to model the PCA-reconstructed PSF at the position of each galaxy in each exposure, based on the GL eigenfunction decomposition. Note that, as we described in Section 3.3.2, every galaxy is detected in the stacked image, and the galaxy position was first defined in the pixel coordinates of the stacked image. The coordinate transformation between the pixel coordinates of the stacked image and a given exposure image is given via the WCS, which is provided by the HSC pipeline. The coordinate transformation differs for the different exposures. Hence we perform the PSF modeling in the celestial coordinates; the model for the PCA PSF at the galaxy position and for the  $\eta$ -th exposure image is given as

$$I^{*(\eta)}(\boldsymbol{\theta}^{(\eta)}) = \sum_{p,q} l_{pq}^{*(\eta)} \psi_{pq}^{\sigma_s^{(\eta)}} \left( \mathcal{W}^{(\eta)}(\boldsymbol{\theta}^{(\eta)} - \boldsymbol{\theta}_0^{(\eta)}) \right), \quad (5)$$

<sup>6</sup> <http://irsa.ipac.caltech.edu/applications/DUST/>

<sup>7</sup> <http://www.cfht.hawaii.edu/~arnouts/LEPHARE/lephare.html>

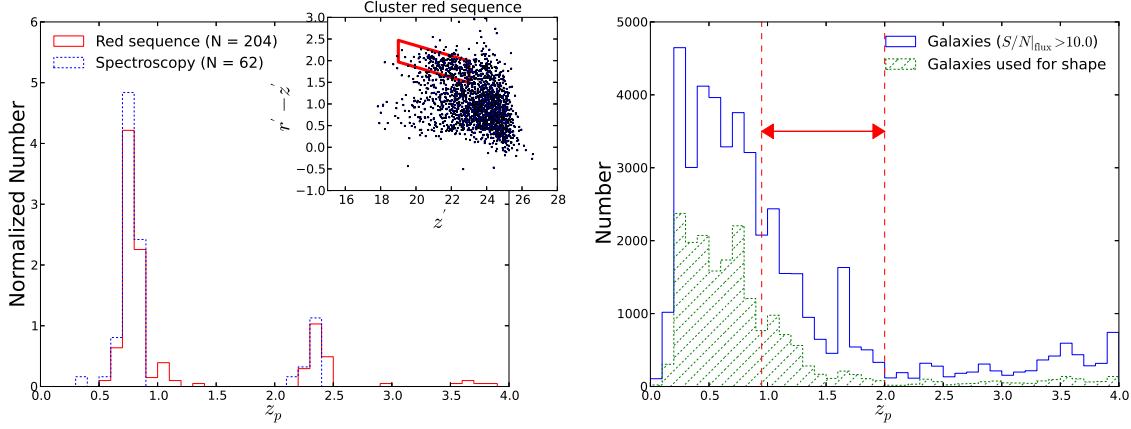


**Figure 3.** *Left panel:* The solid-line histogram shows the distribution of the selected red-sequence galaxies in the ACTJ0022 field, as a function of their photometric redshift estimates  $z_p$  ( $x$ -axis). The red-sequence galaxies are selected by the solid-line box in the color-magnitude diagram, as shown in the inset plot. For comparison, the dotted-line histogram is the distribution of the confirmed cluster members, again as a function of our photo- $z$  estimates of the galaxies, where the spectroscopic redshifts of cluster members are taken with Gemini/GMOS and confirmed to be at the same redshift of the cluster within 5000 km/s. Note that the amplitudes of the histograms are normalized so that  $\sum_i^{\text{bins}} N_{z_p,i} \Delta z = 1$ , where  $\Delta z = 0.1$ . These photo- $z$ s are consistent with the cluster redshift of  $z = 0.81$ , although there are some catastrophic failures at  $z > 2.0$ . *Right panel:* The solid-line histogram shows the photo- $z$  distributions of all the imaging galaxies that have  $S/N > 10$  for the  $3''$  aperture flux in their stacked  $i'$  images. The dotted-line and shaded histogram is the photo- $z$  distribution for the galaxies used for the weak lensing analysis, where the size and flux cut are imposed on those galaxies to have a reliable shape measurement. In our weak lensing analysis, we further impose the photo- $z$  cut  $0.95 < z_p < 2.0$ , which is denoted by dashed vertical lines and a solid arrow, to minimize contamination from the photo- $z$  outliers indicated in the left panel.

where  $\psi_{pq}^{\sigma_*^{(\eta)}}(\boldsymbol{\theta})$  is the two-dimensional (circular) GL function with the order  $(p, q)$ ;  $\sigma_*$  is a parameter to determine the width of the GL functions;  $\mathbf{b}^{*(\eta)}$  is the expansion coefficients; the operation  $\mathcal{W}^{(\eta)}(\boldsymbol{\theta} - \boldsymbol{\theta}_0)$  transforms the pixel coordinate in the  $\eta$ -th exposure to the celestial coordinates;  $\boldsymbol{\theta}_0$  is the centroid of the PSF. Thus, by modeling the PSF in the celestial coordinates, we properly correct for the astrometric distortion effect, which is treated as a coordinate transformation, not a convolution effect, e.g. in the case for the atmospheric smearing effect (the major part of PSF).

The fitting parameters of Eq. (5) are  $(b_{pq}^*, \sigma_*, \boldsymbol{\theta}_0)$ . We employ the  $\chi^2$  fitting via  $\chi^2 = \sum_{\alpha} [I_{\text{data}}^*(\boldsymbol{\theta}_{\alpha}) - I^*(\boldsymbol{\theta}_{\alpha})]^2 / \sigma_{\alpha}^2$ , to determine the model parameters. The  $\chi^2$  minimization with respect to the parameters  $b_{pq}^*$  can be reduced to a linear algebra problem, so  $b_{pq}^*$  can be uniquely determined for given  $\sigma_*$  and  $\boldsymbol{\theta}_0$ , thanks to the orthogonality of the eigenfunction. Hence we need to find the best-fit  $\sigma_*$  and  $\boldsymbol{\theta}_0$  by minimizing the  $\chi^2$ -value, at the galaxy position in each exposure.

As an estimate of the accuracy of our PSF measurement, we compare the size and ellipticities of each star image with those of the PCA-reconstructed PSF image at the star position. Using the best-fit  $\mathbf{b}^*$  coefficients, the size and conformal shear of objects can be estimated (Bernstein & Jarvis 2002) as

$$\begin{aligned} \tilde{\sigma}^* &= \sigma^* \exp\left(\frac{b_{11}^*}{b_{00}^* - b_{22}^*}\right), \\ \boldsymbol{\eta} &= \frac{2\sqrt{2}b_{02}^*}{b_{00}^* - b_{22}^*}. \end{aligned} \quad (6)$$

Then we convert  $\boldsymbol{\eta}$  to the reduced shear as  $g = \tanh(\boldsymbol{\eta}/2)$ . Fig. 4 shows the results for this comparison. Note that we performed the same fitting described in the earlier part of this section for each star image to obtain the best-fit  $\mathbf{b}^*$  coefficients. The fractional size difference between the PCA-PSF and star sizes agrees to within 0.2 per cent. The typical residual of ellipticities on each chip is  $\mathbf{g}^* - \mathbf{g}^{\text{PSF}} = (1.4 \pm 6.5, 0.6 \pm 6.4) \times 10^{-4}$  (the mean and RMS

in the chip averaged over the different exposures), and is consistent with zero. These residuals would contaminate galaxy shapes as an additive bias. We will discuss the impact on the cluster mass estimation from the measured weak lensing signal in Section 4.2.

### 3.4.3 Galaxy shape measurement

For simultaneous multi-exposure fitting of a given galaxy shape, we use the same model parameters for different images in different exposures. Note that the internal astrometric errors are typically  $\sim 0.01''$ , as describe in Section 3.3.1. Hence we believe that the coordinate transformations between different exposures are known accurately enough, and the astrometric errors do not induce a significant systematic error in the lensing shear estimate (less than 1 per cent; see Miyatake in prep.).

In our fitting procedure, we first estimate a size for the PSF-convolved image of a given galaxy, by combining the different exposures based on the GL eigenfunction decomposition:

$$\chi^2 = \sum_{\eta}^{N_{\text{exp}}} \sum_{\alpha}^{N_{\text{pix}}^{(\eta)}} \frac{\left[ f_s^{(\eta)} I^{(\eta)}(\boldsymbol{\theta}_{\alpha}^{(\eta)}) - \sum_{p,q} b_{pq}^{(\eta)} \psi_{pq}^{\sigma_o^{\text{ini}} E}(\mathcal{W}^{(\eta)}(\boldsymbol{\theta}_{\alpha}^{(\eta)} - \boldsymbol{\theta}_0^{(\eta)})) \right]^2}{\left( f_s^{(\eta)} \sigma_{\alpha}^{(\eta)} \right)^2}, \quad (7)$$

where  $\alpha$  runs over pixels in the segmentation region around the galaxy (see Section 3.3.2);  $\sigma_{\alpha}^{(\eta)}$  is the sky noise at the position  $\boldsymbol{\theta}_{\alpha}$  of the  $\eta$ -th exposure;  $f_s^{(\eta)}$  is the scaling factor of the exposure estimated by the HSC pipeline (Section 3.3.1); and  $\psi_{pq}^{\sigma_o^{\text{ini}} E}$  are elliptical GL functions that have width  $\sigma_o^{\text{ini}}$ , for which we use  $\sigma_o^{\text{ini}} = 1.49$  pixels as the initial guess. Following the method in Nakajima & Bernstein (2007), a galaxy image is modelled in a



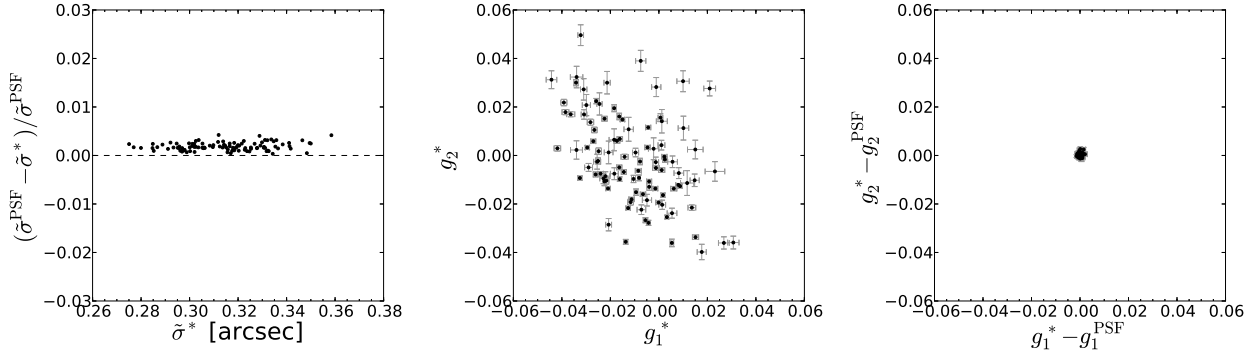


**Figure 4.** *Left panel:* The fractional differences between the sizes of the PCA-reconstructed PSFs and star images as a function of the star size (see Eq. 6 for the size definition). Each dot denotes the mean values measured from each CCD chip (we have 100 results in total, 10 CCD chips times 10 exposures). The dashed line denotes the relation  $\hat{\sigma}^{\text{PSF}} = \hat{\sigma}^*$ . *Middle panel:* The measured ellipticities of stars in each CCD. Each dot with error bars denotes the mean value of the ellipticities of stars lying in a given chip, and the error bars are the standard deviation. *Right panel:* Similar to the middle panel, but for the residual ellipticities between the stars (in the middle panel) and the PCA-reconstructed PSFs. Here, in each chip, we measured ellipticities of the PCA-reconstructed PSF at each star position, subtracted the observed star ellipticity, and computed the mean and standard deviation (see Section 3.2.3 for the PCA-PSF determination). Note that we measured the size and ellipticities using the Gauss-Laguerre shapelet method (see Section 3.4.1).

sheared coordinate system rather than in the sky plane, because the lensing shear distortion is equivalent to an elliptical coordinate transformation. More precisely, the elliptical GL functions are defined as

$$\psi_{pq}^{\sigma E}(\boldsymbol{\theta}) \equiv \psi_{pq}^{\sigma}(\mathbf{E}^{-1}\boldsymbol{\theta}), \quad (8)$$

$$\mathbf{E}^{-1} \equiv \frac{e^{-\mu}}{\sqrt{1-g^2}} \begin{pmatrix} 1-g_1 & -g_2 \\ -g_2 & 1+g_1 \end{pmatrix}. \quad (9)$$

Here  $\mathbf{E}$  represents a coordinate transformation from the sky plane that includes a two-dimensional translation, a shear  $\mathbf{g}$ , and a dilution  $\mu$ . There are 5 fitting parameters,  $(\mu, g_1, g_2, x_c, y_c)$ , where  $(x_c, y_c)$  is the centroid position of the galaxy. Following Nakajima & Bernstein (2007), we minimize  $\chi^2$  so that the obtained coefficients  $b_{pq}$  satisfy the so-called “null test” given by  $b_{10} = b_{01} = b_{11} = b_{20} = b_{02} = 0$ . This  $\chi^2$ -minimization gives an estimate of the size of the *observed* galaxy as  $e^{\mu}\sigma_{\alpha}^{\text{ini}}$ , which includes the PSF smearing effect. We define  $\sigma_{\text{gal}} = (e^{\mu}\sigma_{\alpha}^{\text{ini}})^2 - \sigma_*^2$  to estimate the size of the pre-seeing galaxy image as the initial guess, where  $\sigma_*^2$  is the harmonic mean of the PSF sizes over different exposures. Note that, similarly to the PSF fitting, we account for the astrometric distortion by performing the fitting in the celestial coordinates.

Then, by using the coefficients  $b_{pq}^*$  obtained from the PSF estimation in Section 3.4.2, we estimate the ellipticity of the pre-seeing galaxy image for each galaxy by minimizing

$$\chi^2 = \sum_{\eta=1}^{N_{\text{exp}}} \sum_{\alpha=1}^{N_{\text{pix}}^{(\eta)}} \frac{\left[ f_s^{(\eta)} I^{(\eta)}(\boldsymbol{\theta}_{\alpha}^{(\eta)}) - \sum_{p,q} b_{pq} \phi_{pq}^{\sigma_{\alpha} E}(\mathbf{b}^{*(\eta)}; \boldsymbol{\mathcal{W}}^{(\eta)}(\boldsymbol{\theta}_{\alpha}^{(\eta)})) \right]^2}{\left( f_s^{(\eta)} \sigma_{\alpha}^{(\eta)} \right)^2}, \quad (10)$$

where  $\phi_{pq}^{\sigma_{\alpha} E}(\mathbf{b}^{*(\eta)}; \boldsymbol{\theta})$  are the basis functions including the PSF convolution effect, defined as

$$\phi_{pq}^{\sigma_{\alpha} E}(\mathbf{b}^*; \boldsymbol{\theta}) = \left[ \psi_{pq}^{\hat{\sigma}_{\text{gal}} E} \otimes \sum_{p^*, q^*} b_{p^* q^*}^* \psi_{p^* q^*}^{\sigma_*} \right](\boldsymbol{\theta}). \quad (11)$$

The convolution in the above equation can be done analytically. Following Nakajima & Bernstein (2007) and using the initial guess of the galaxy size  $\sigma_{\text{gal}}$  obtained from Eq. (7), we do not vary the dilution parameter  $\mu$  and fix the galaxy size parameter  $\hat{\sigma}_{\text{gal}}$  in the above equation to  $\hat{\sigma}_{\text{gal}}^2 = \sigma_{\text{gal}}^2 + (f_p - 1)\sigma_*^2$ , where we set  $f_p = 1.2$ . Thus we used the slightly widened size parameter than expected from the initial guess,  $\sigma_{\text{gal}}$ , because in Nakajima & Bernstein (2007) it is shown that this choice results in more sensitive measure of the input shear in image simulations. Again, by imposing the “null test” conditions, we minimize the above  $\chi^2$  in order to estimate the ellipticity parameter  $\mathbf{g}$  for the galaxy, which is used for weak lensing shear estimation.

Using the best-fit  $\mathbf{b}$  coefficients, we can estimate the total signal-to-noise ratio or significance for measuring the flux of each galaxy image (Bernstein & Jarvis 2002):

$$\nu = \frac{f}{\sqrt{\text{Var}(f)}}, \quad (12)$$

where the flux is defined in terms of the coefficients  $b_{pq}$  as  $f \equiv \sum_p b_{pp}$ . The variances or uncertainties of the coefficient,  $\text{Var}(f)$ , can be properly estimated by propagating the sky noise  $\sigma_{\alpha}$  into the parameter estimation. We set the order of Gauss-Laguerre function for galaxy fitting to 2 and that for PSF fitting to 8, in order that the fit will converge even for noisy images. The shear recovering accuracy test for this set up is described below.

Using image simulations, we have tested the robustness of our shape measurement. To be more precise, we used the elliptical exponential profile for a model galaxy image. For modelling a star image, we used double Gaussian functions:

$$I^*(r; \sigma, f_I, f_{\sigma}) \equiv G(r; \sigma) + f_I G(r; f_{\sigma} \sigma) \quad (13)$$

$$G(r; \sigma) \equiv e^{-\frac{r^2}{2\sigma^2}}, \quad (14)$$

where  $G(r; \sigma)$  is an unnormalized Gaussian profile with width  $\sigma$ , and we used  $\sigma = 0.75'' / 2\sqrt{2 \log(2)}$  corresponding to  $0.75''$  in FWHM and  $(f_I, f_{\sigma}) = (0.1, 2.0)$ . We also included Gaussian noise in the simulated images, as a model of the sky noise. We studied the accuracy to which we can recover the input weak lensing shear as a function of the flux  $S/N$  and size of simulated galaxy

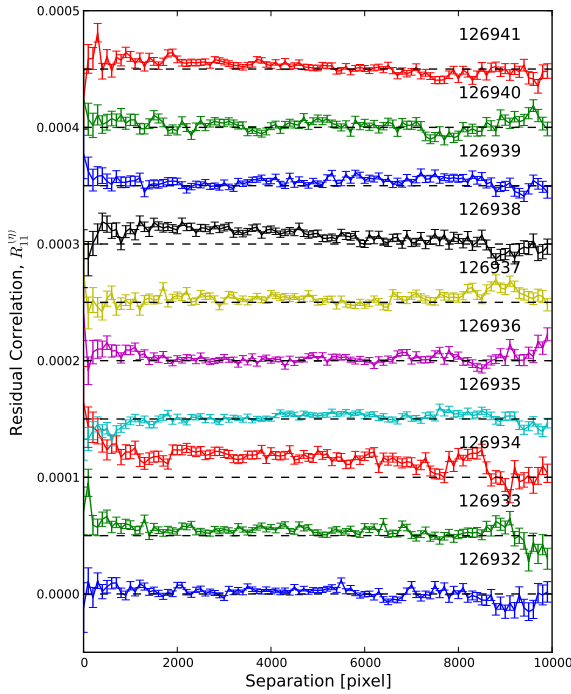


**Figure 5.** The residual correlation function (Eq. 15) between the tangential components of the star ellipticities and the galaxy ellipticities, against separation angle between the star and galaxy pair. Note that the tangential shear components are defined with respect to the vector connecting star and galaxy in each pair, not with respect to the cluster center. For the galaxy ellipticity, we used the difference between the galaxy ellipticities measured by combining all the 10 exposures or the 9 exposures removing a particular one exposure denoted by the label ID (e.g., 126932 for the first exposure). Hence the data with error bars show the 10 different correlation functions. For illustrative clarity, the functions except for the first exposure 126932 are vertically shifted (stepped by  $5.0 \times 10^{-5}$  for each curve), and the dashed line around each result denotes the zero amplitude.

images. We have found that, in order to have a relative accuracy of shear better than 10 per cent,  $|\delta\gamma/\gamma| \leq 0.1$ , we need to use galaxies satisfying  $\nu > 20$  and  $\sigma_{\text{gal}} > 1.2$  pixels. The final number density becomes  $3.2 \text{ arcmin}^{-2}$ . Hence, in the following weak lensing analysis, we further impose these conditions for galaxy selection, and will come back to this issue to discuss how the shear recovery accuracy will affect the mass estimate in Section 4.2.

#### 3.4.4 Residual Correlation

One of the great advantages of the multi-exposure fitting is that we keep the PSF information in each exposure. In this section, we study diagnostics for identifying an exposure that may not be suitable for shape measurement, either in terms of data quality or inaccuracy of PSF estimation, e.g. due to too rapidly-varying PSF patterns that cannot be handled by the chosen PSF modeling algorithm. For this purpose, we consider the following correlation

function between the ellipticities of galaxies and stars:

$$R_{ij}^{(\eta)}(\theta) \equiv \left\langle e_i^{\text{star},(\eta)}(\theta') \times \left( e_j^{\text{gal},(\text{all})}(\theta' + \theta) - e_j^{\text{gal},(\text{all}-\eta)}(\theta' + \theta) \right) \right\rangle, \quad (15)$$

where  $\langle \dots \rangle$  denotes the average for all the pairs separated by the angle  $\theta$ ;  $e_i^{\text{star},(\eta)}(\theta')$  is the  $i$ -th ellipticity component of star at the position  $\theta'$  for the  $\eta$ -th exposure;  $e_i^{\text{gal},(\text{all})}(\theta' + \theta)$  is the ellipticity component of galaxy at the position  $\theta' + \theta$ , measured by combining all the exposures;  $e_i^{\text{gal},(\text{all}-\eta)}(\theta' + \theta)$  is the ellipticity measured by combining the exposures except for the  $\eta$ -th exposure. Although the correlation between star and galaxy ellipticities is often used in the literature as a diagnostic of the imperfect shape measurement, the above correlation can be more useful for identifying problems with some particular exposure, as explained below.

Suppose that the  $\eta$ -th exposure has a systematic error in the PSF estimation. In this case,  $e_i^{\text{gal},(\text{all})}(\theta)$  may have some contamination from the imperfect PSF estimation in the  $\eta$ -th exposure, while  $e_i^{\text{gal},(\text{all}-\eta)}(\theta)$  does not have the contamination. The difference  $[e_i^{\text{gal},(\text{all})}(\theta) - e_i^{\text{gal},(\text{all}-\eta)}(\theta)]$  is sensitive only to the PSF estimation of the  $\eta$ -th exposure. Hence, if the imperfect PSF estimation is really a problem, the ellipticity difference may have a non-vanishing correlation with the PSF ellipticity of the  $\eta$ -th exposure,  $e_i^{\text{star},(\eta)}(\theta)$ . This is what the correlation (Eq. 15) tries to measure. Hereafter we call this the *residual correlation*. Its advantage over a direct correlation is that, in such small fields as these, the PSF ellipticity can easily correlate with the real lensing shear; such an effect cancels out of the difference in the residual correlation, but would contribute to a standard star-galaxy correlation function.

Since we have 10 different exposures for the  $i'$ -band image of the ACTJ0022 data, we have 10 different correlation functions to test the accuracy of PSF estimation in each exposure. Fig. 5 shows the results. The figure clearly shows that one exposure with ID “126934” shows non-zero correlations over all the range of separation angles, indicating that the exposure has some systematic issue in the PSF estimation. In fact, we found that the PSF in this exposure exhibits larger ellipticities, typically  $e \sim 0.04$ , than in other exposures. Although we have checked that the weak lensing tangential shear signal is not significantly affected even when including the exposure in the analysis, we do not use the 126934 exposure in the following analysis<sup>8</sup>. One may notice that the other residual correlations show non-vanishing correlations with amplitude  $\sim 10^{-5}$  at some scales. Since the ellipticity difference,  $[e_i^{\text{gal},(\text{all})}(\theta) - e_i^{\text{gal},(\text{all}-\eta)}(\theta)]$ , arises naively from the star ellipticities in the  $\eta$ -th exposure, the residual correlation would scale as  $(e^{\text{star},(\eta)})^2$ . In turn, if the galaxy ellipticity is affected by the imperfect PSF correction inferred by the residual correlations, the contamination to the cluster lensing would be of the order of  $e^{\text{star},(\eta)} \simeq \sqrt{R} \sim 0.003$ , which is more than one order magnitude smaller than the cluster lensing. Hence we do not believe that the residual PSF systematic error, even if it exists, should affect the following weak lensing analysis (see later for further discussion on the impact of imperfect PSF estimation).

<sup>8</sup> One might be concerned that the nonzero residual correlation suggests that we should not trust the PSF size estimate, which could give rise to a multiplicative bias in the shear.

## 4 RESULTS

### 4.1 Cluster Mass

We can now combine the photo- $z$  estimate and shape measurement for each background galaxy to estimate the weak lensing signal of ACTJ0022. In this paper, we focus on the tangential shear component, defined as

$$g_+ = -(g_1 \cos 2\phi + g_2 \sin 2\phi), \quad (16)$$

where  $\phi$  is the position angle between the 1st coordinate axis and the vector connecting the galaxy position and the cluster center for which we use the BCG position. Similarly, we can define the component,  $g_\times$ , from the 45 degrees rotated ellipticity component from  $g_+$ .

To estimate the weak lensing signal due to ACTJ0022, we compute the radial profile by averaging the measured tangential ellipticities of background galaxies in each circular annulus as a function of the cluster-centric radius:

$$\langle e_+(\theta_n) \rangle = \frac{1}{\mathcal{R}} \frac{\sum_i w_i e_{+,i}}{\sum_i w_i}, \quad (17)$$

where  $w_i$  is the weight for the  $i$ -th galaxy, the summation  $\sum_i$  runs over all the galaxies lying in the  $n$ -th annulus with radii  $\theta_{n,\text{in}} \leq \theta \leq \theta_{n,\text{out}}$ , and  $\mathcal{R}$  is the shear responsivity. To compute  $w_i$  and  $\mathcal{R}$ , we used Eqs. (5.33), (5.35) and (5.36) in Bernstein & Jarvis (2002). Note that, for the central value of each radial bin, we infer the area-weighted mean radius of the annulus, i.e.  $\theta_n \equiv \int_{\theta_{n,\text{in}}}^{\theta_{n,\text{out}}} 2\pi r^2 dr / \int_{\theta_{n,\text{in}}}^{\theta_{n,\text{out}}} 2\pi r dr$ . Similarly we estimate the statistical uncertainty of the measured signal in each radial bin:

$$\sigma_{e_+}(\theta_n) = \frac{1}{\mathcal{R}} \sqrt{\frac{\sum_i w_i^2 e_{+,i}^2}{(\sum_i w_i)^2}}. \quad (18)$$

Here we have assumed that the statistical uncertainty arises solely from the intrinsic ellipticities of source galaxies per component. Recalling that the relation between the ellipticity ( $e$ ) and the shear ( $g$ ) is given as  $e = \tanh(2 \tanh^{-1} g)$ , where  $e = \sqrt{e_+^2 + e_\times^2}$  and so on, we can convert the measured ellipticities to the lensing shear components; e.g.,  $g_+ = (g/e)e_+$ .

Fig. 6 shows the measured radial profiles for the tangential shear and the 45-degree rotated component for ACTJ0022. The figure clearly shows the coherent signals for  $g_+$ , where the amplitudes are increasing with decreasing radius as expected for cluster lensing. On the other hand, the non-lensing mode  $g_\times$ , which can serve as a monitor of the residual systematic effects, is consistent with zero over the range of radii we consider. Note that we plot the  $g_\times$ -profile in units of  $\theta_n \times g_\times(\theta_n)$  so that the scatter in the values is independent of radius for logarithmically-spaced binning, if the measurement errors in the  $g_+/g_\times$  signals arise from the random intrinsic shapes<sup>9</sup>. However, the shear measurement is still noisy, mainly due to the small number density of source galaxies (3.2 arcmin<sup>-2</sup>). If we estimate the total  $S/N$  for the shear measurement as  $(S/N)^2 \equiv \sum_n [(g_+(\theta_n))/\sigma_+^2(\theta_n)]$ , we find  $S/N \simeq 3.7$ , i.e. about  $3.7\sigma$  detection of the lensing signal.

<sup>9</sup> The number of background galaxies in each annulus scales with radius as  $N_g \propto \theta_n^2 \Delta \ln \theta$  for the logarithmically-spaced binning. The shape noise contribution to the statistical errors of the  $g_+/g_\times$  measurements scale as  $\sigma(g_{+, \times}) \propto \sigma_e^2 / \sqrt{N_g} \propto 1/\theta_n$ . Hence  $\theta_n \sigma(g_{+, \times})$  becomes independent of radius.

	setup	$M_{200}$ [ $10^{15} M_\odot/h$ ]	$c_{200}$	$\chi^2/\text{d.o.f.}$
Case 1	$c_{200}$ : free	$0.75^{+0.32}_{-0.28}$	$> 9.7$	4.38/5
Case 2	$c_{200} = 4.0$	$0.85^{+0.35}_{-0.44}$	fixed	7.29/6

**Table 3.** Results for the NFW profile fitting to the measured tangential shear profile for ACTJ0022 shown in Fig. 6.

We now estimate the cluster mass of ACTJ0022 by comparing the measured shear signal to the model lensing profile expected from the Navarro-Frenk-White (NFW) profile (Navarro et al. 1996). The NFW profile is given as  $\rho_{\text{NFW}} = \rho_s / [(r/r_s)(1 + r/r_s)^2]$  and specified by two parameters ( $\rho_s, r_s$ ). We can rewrite the NFW profile to be specified by the enclosed mass  $M_\Delta$  and the concentration parameter  $c_\Delta$  (e.g. see Okabe et al. 2010, for the conversion). The cluster mass often used in the literature is the three-dimensional mass enclosed within a spherical region of a given radius  $r_\Delta$  inside of which the mean interior density is  $\Delta$  times the mean mass density at the cluster redshift,  $\bar{\rho}_m(z_l)$ :

$$M_\Delta = \frac{4\pi}{3} r_\Delta^3 \bar{\rho}_m(z_l) \Delta. \quad (19)$$

Note that, in this analysis, we are working in physical distance units. The concentration parameter is defined by  $c_\Delta = r_\Delta/r_s$ . For most of this paper, we use  $\Delta = 200$ . Alternatively, the cluster mass can be defined in terms of the critical density  $\rho_c$  instead of  $\bar{\rho}_m$ , in which case we denote the mass as  $M_{\Delta\rho_c}$  in the following.

Given the NFW profile, we can analytically compute the expected radial profiles of the lensing fields (Bartelmann 1996; Wright & Brainerd 2000). For example, the lensing convergence profile, which is equivalent to the radial profile of the projected mass density, is computed as

$$\kappa_{\text{NFW}}(\theta) \equiv \Sigma_{\text{cr}}^{-1} \int_{-\infty}^{\infty} dr_{\parallel} \rho_{\text{NFW}} \left( \sqrt{r_{\parallel}^2 + (D_l \theta)^2} \right), \quad (20)$$

where  $\Sigma_{\text{cr}}$  is the critical surface mass density (see below) and  $D_l$  is the angular diameter distance to the cluster redshift. The projection integration in the above equation can be analytically done. Similarly the shear profile  $\gamma_{\text{NFW}}(\theta)$  can be analytically derived. The measured shear profile  $g_+(\theta)$  is the reduced shear (Bartelmann & Schneider 2001), and is given as  $g_+(\theta) = \gamma_{\text{NFW}}(\theta)/(1 - \kappa_{\text{NFW}}(\theta))$  for an NFW profile. The critical surface mass density is given as

$$\Sigma_{\text{cr}} = \frac{c^2}{4\pi G} D_l^{-1} \left\langle \frac{D_{ls}}{D_s} \right\rangle^{-1}, \quad (21)$$

where  $D_l$ ,  $D_s$ , and  $D_{ls}$  are angular diameter distances from observer to cluster (lens), from observer to source, and from cluster to source. The mean distance ratio is calculated using the photo- $z$  estimates of source galaxies as

$$R \equiv \left\langle \frac{D_{ls}}{D_s} \right\rangle = \frac{\sum_i w_i [1 - D_l/D(z_{\text{phz},i})]}{\sum_i w_i}, \quad (22)$$

where the summation runs over all the source galaxies and  $w_i$  is the weight used when calculating the shear profile. Note the average above is equivalent to the average  $\langle 1/D(z_s) \rangle$ , as the cluster redshift (lens redshift) is known.

We estimate the cluster mass  $M_\Delta$  by minimizing the following  $\chi^2$  with varying the model parameters ( $M_\Delta, c_\Delta$ ):

$$\chi^2 = \sum_n \frac{[\langle g_+(\theta_n) \rangle - g_{\text{NFW}}(\theta_n; M_\Delta, c_\Delta)]^2}{\sigma_{g_+}(\theta_n)^2}. \quad (23)$$

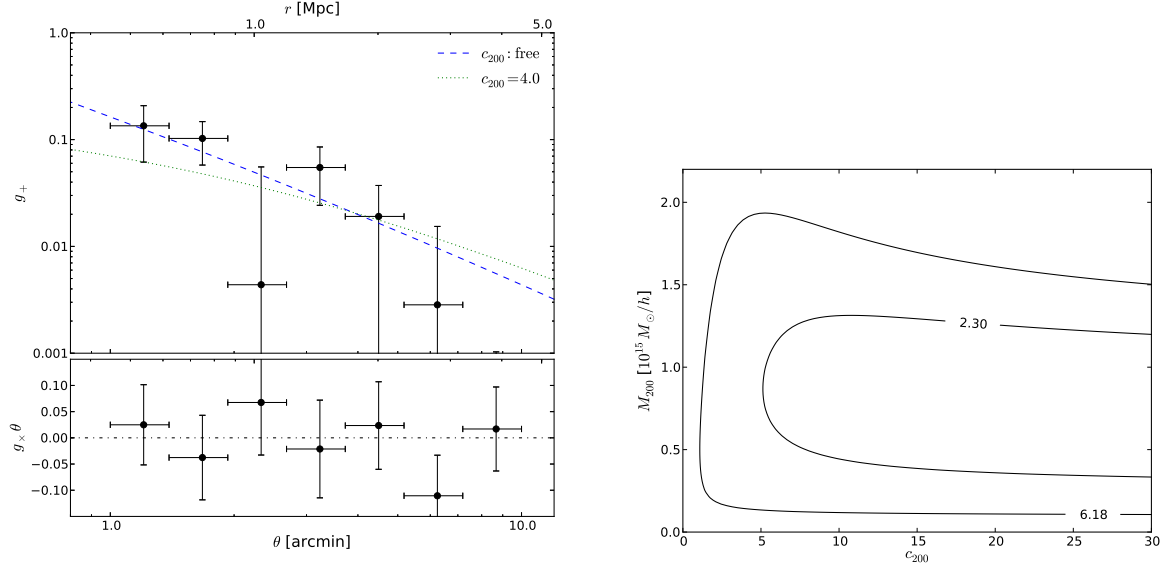


**Figure 6.** *Left panel:* The measured radial profiles of tangential shear component (upper plot) and its 45-degree rotated component, non-lensing mode (lower plot). The vertical error bar around each data point shows the  $1\sigma$  statistical error in each radial bin, while the horizontal error bar denotes the bin width. The dashed curve shows the best-fit NFW profile, while the dotted curve is the best-fit NFW when fixing the concentration parameter to the  $\Lambda$ CDM model expectation,  $c_{200} = 4.0$  (see text for details). The non-lensing B-mode,  $g_{\times}$ , is consistent with zero over a range of the radial bins we consider. *Right panel:* The  $\Delta\chi^2$  contours in  $(M_{200}, c_{200})$  plane for the NFW profile fitting where the concentration parameter is allowed to vary. The two lines correspond to  $\Delta\chi^2 = 2.30$  (68% C.L.) and 6.18 (95% C.L.), respectively.

We consider two cases for the NFW fitting: For Case 1, we allow the concentration parameter to be free; for Case 2, we fixed it to  $c_{200} = 4.0$ , which is a theoretically-expected  $1\sigma$  upper bound on the concentration parameter for a cluster with  $M_{200} = 10^{15} M_{\odot}/h$ . To be more precise, the fitting formula derived in Duffy et al. (2008) using N-body simulations for a  $\Lambda$ CDM model gives  $c_{200} \simeq 3.2$  for a cluster with  $M_{200} = 10^{15} M_{\odot}/h$  and at  $z = 0.81$ . Since the Subaru WL prefers a steeper NFW profile (therefore with the higher  $c_{200}$ ) for ACTJ0022 as we will discuss below, we adopt the  $1\sigma$  upper bound of  $c_{200} = 4.0$  motivated by the fact that the simulations show typical intrinsic scatters of  $\sigma(c_{200}) \simeq 1$  for such massive halos.

Table 3 shows the results for the two cases, and the left panel of Fig. 6 shows the best-fit NFW profiles compared with the measurement. For Case 1, we cannot constrain the concentration parameter, and obtained only the  $1\sigma$  lower bound as  $c_{200} \geq 9.7$ , because the measured shear profile does not show a clear curvature over the range of radii we probe. The lower bound also means that the measured shear profile is consistent with the outer part of NFW profile,  $\rho_{\text{NFW}} \propto r^{-3}$ . This can be explained as follows. The best-fit virial radius  $r_{200} \simeq 1.8$  Mpc indicates the NFW scale radius  $r_s \sim 0.5$  Mpc if we assume the concentration parameter  $c \sim 4$ , the  $\Lambda$ CDM prediction. As shown in Fig. 6, the shear signals at radii smaller than 0.5 Mpc are not available, meaning that we cannot probe the inner part of the expected NFW profile from the measured shear signal and constrain the concentration parameter from the varying slope of the profile. If strong lensing signals are available for the inner regions, we may be able to constrain the concentration parameter as done in Broadhurst et al. (2005), but we have not found any strongly-lensed candidates in the cluster region.

For Case 2, we found a slightly larger best-fit mass than in Case 1, because the concentration parameter is fixed to  $c_{200} = 4.0$ , which is smaller than the  $1\sigma$  lower bound for Case 1, and a larger

mass is needed to explain the measured shear amplitude with the small  $c_{200}$  (see the right panel of Fig. 6). However, the difference between the best-fit cluster masses for Case 1 and 2 is within the error bars, so not significant.

## 4.2 Systematic Uncertainties from Measurement

In this section, we discuss the impact of several systematic errors on the cluster mass estimation.

### 4.2.1 Imperfect shape measurement

First, we consider systematic error due to imperfect shape measurement. To estimate the impact, as described in Section 3.4.1, we have carried out many image simulations as a function of different flux  $S/N$  values and the different galaxy size parameters for simulated galaxy images. We considered  $\nu = 20, 27, 60, 130$  and  $\sigma_{\text{gal}} = 1.3, 1.4, 1.8, 2.2, 2.7$  pixels, in total 20 different image simulations. For each simulation that contains 80000 galaxies, we tested whether our shear method can recover the input shear. For each simulation, we quantify the systematic error found from the image simulations in terms of a multiplicative bias parameter  $m$ :  $\gamma_{\text{recovered}} = (1 + m)\gamma_{\text{input}}$ . We have found that our method leads to a 1 per cent to 10 per cent bias, or  $m = 0.01 - 0.1$ , where  $m$  is determined within relative accuracy of  $\sim 10$  per cent. Then, we averaged the simulation results for the estimated bias by weighting the result of each simulation with the number density of galaxies used for our actual ACTJ0022 analysis that fall into the similar region of the flux  $S/N$  and size values of each simulation. As a result, we found the average multiplicative bias  $m \simeq -0.06$  for the background galaxies of ACTJ0022, implying that our method tends to underestimate the true shear value and therefore underestimate the cluster mass.

### 4.2.2 Photo- $z$ errors

We study how photo- $z$  errors used in selecting background galaxies affect the cluster mass estimate. There are two effects to be considered: (1) a dilution of the lensing signals caused by an inclusion of unlensed galaxies into the background galaxy sample, and (2) inaccuracy in estimating the mean critical mass density  $\Sigma_{cr}$  from the photo- $z$ s (Eq. 21).

For the dilution effect, the correction factor is estimated from the fraction of galaxies whose true redshifts are lower than the cluster redshift 0.81:

$$f_c \equiv \frac{N_{\text{sel},z_p}(z_s < 0.81)}{N_{\text{sel},z_p}}, \quad (24)$$

where  $z_s$  is the true redshift, and  $N_{\text{sel},z_p}$  is the total number of galaxies in the background galaxy catalog. We checked that the radial profile of number densities of the background galaxies does not show any radial dependence, i.e. no clear indication of the contamination of unlensed cluster member galaxies. Nevertheless, we here address an effect of possible residual contamination from foreground galaxies on the lensing signal. If the contamination is uniform over the ACTJ0022 field, as indicated by the number density profile, the measured shear is diluted as

$$\langle g^{\text{meas}} \rangle = (1 - f_c) \langle g^{\text{true}} \rangle, \quad (25)$$

where  $\langle g^{\text{meas}} \rangle$  and  $\langle g^{\text{true}} \rangle$  are the measured and underlying-true shear signals, respectively. If  $f_c > 0$ , the measured shear signal is affected by the dilution, and therefore underestimated. The true shear and the true cluster mass should be higher than inferred from the measurement.

For inaccuracy in the  $\Sigma_{cr}$  estimation, the correction factor can be estimated as

$$R^{\text{true}} \equiv \frac{\int_{z_{\text{lens}}}^{\infty} dz_s \frac{dN_{\text{sel},z_p}^{\text{true}}}{dz_s} \frac{D_{ls}(z_s)}{D_s(z_s)}}{\int_{z_{\text{lens}}}^{\infty} dz_s \frac{dN_{\text{sel},z_p}^{\text{true}}}{dz_s}}, \quad (26)$$

where  $dN^{\text{true}}/dz_s$  is the underlying true redshift distribution of the background galaxies. The question is whether the quantity  $R$ , estimated based on the photo- $z$ s (Eq. 22), may differ from the true value  $R^{\text{true}}$  due to the photo- $z$  errors. If there is a bias in  $R$ , denoted as  $R = R^{\text{true}} + \delta R$ , the NFW profile to be compared with the measured shear profile is biased as

$$g_{\text{NFW}}^{\text{phz}} \equiv g_{\text{NFW}}^{\text{true}} (1 + \delta R/R^{\text{true}}), \quad (27)$$

where  $g_{\text{NFW}}^{\text{phz}}$  is the model NFW inferred from the photo- $z$  information of every galaxy and  $g_{\text{NFW}}^{\text{true}}$  is the model NFW profile using the true distance ratio. If  $\delta R > 0$ , the model NFW amplitude is overestimated, and then the best-fit mass would be underestimated in order to reproduce the measured shear amplitude. Hence the true mass should be higher than inferred.

To estimate possible biases in the factors  $f_c$  and  $R$ , we used the publicly available COSMOS photo- $z$  catalog assuming that the photo- $z$ s derived by using 30 broad, intermediate and narrow-band data are true redshifts (Ilbert et al. 2009). We obtain the photo- $z$  distribution for the COSMOS galaxies by applying our photo- $z$  method to the COSMOS  $Br'i'z'$  magnitudes of each galaxy to estimate its photo- $z$ . Note that the COSMOS catalog does not have the  $Y$ -band data. Since the limiting magnitude of the background galaxies used for the weak lensing analysis ( $i'_{\text{lim}} = 25.6$ ) is shallower than the COSMOS catalog ( $i'_{\text{lim}} = 26$ ), we can reliably use the COSMOS catalog for this purpose. To correct for the limiting

magnitude difference, we use the following equation to estimate the underlying true redshift distribution for the background galaxy sample:

$$\frac{dN_{\text{sel},z_p}^{\text{ACTJ}}}{dz_s} = \frac{dN_{\text{sel},z_p}^{\text{COSMOS}}}{dz_s} \times \frac{dN^{\text{th}}/dz(i < 25.6)}{dN^{\text{th}}/dz(i < 26)} \quad (28)$$

where  $dN^{\text{th}}/dz$  is the fitting formula that gives the redshift distributions as a function of the limiting magnitude in Ilbert et al. (2009). Using the redshift distribution given by Eq. (28), we found that possible biases in the correction factors are  $f_c \simeq 0.10$  or  $\delta R/R^{\text{true}} \simeq -0.07$ , respectively.

The COSMOS photo- $z$  catalog may be affected by cosmic sample variance due to the small area coverage (about 2 deg<sup>2</sup>); the redshift distribution shows non-smooth features due to large-scale structures along the line-of-sight. Hence we also estimate the impact of photo- $z$  errors using the mock catalog used in Nishizawa et al. (2010). In the mock catalog, we properly included the response functions of Subaru  $Br'i'z'Y$  filters we used. We generated the mock catalog such that it reproduces the fitting formula for the redshift distribution of the COSMOS photo- $z$  catalogs in Ilbert et al. (2009) as a function of the  $i'$ -band limiting magnitudes. Note that the fitting formula for the redshift distribution has a smooth functional form against redshift. We also included a mixture of different galaxy SED types according to the COSMOS results. By estimating photo- $z$ s for the mock galaxies and using galaxies down to the limiting magnitude of ACTJ0022, we found biases of 0.15 for  $f_c$  and 0.07 for  $\delta R/R^{\text{true}}$ , respectively.

From the above investigation, we estimate typical bias from inaccurate photo- $z$  estimation to be  $f_c \simeq 0.10$  and  $\delta R/R^{\text{true}} \simeq \pm 0.07$ . Note that we further imposed size and magnitude cuts on the background galaxies for the weak lensing analysis, which preferentially selects brighter galaxies than the limiting magnitude. Hence, the biases inferred here correspond to a maximum bias, because the brighter galaxies have more accurate photo- $z$  and are less contaminated by photo- $z$  outliers.

### 4.2.3 Imperfect PSF estimation

Although we carefully tested for imperfect PSF estimation in Section 3.4.4, here we consider how a residual systematic error in the PSF estimation affects the shear estimation.

First, we consider the impact of the PSF size misestimation as studied in the left panel of Fig. 4, where we found a 0.2 per cent level in the size misestimation. Following the prescription provided by Hirata et al. (2004), we found that the PSF size misestimation of 0.2 per cent corresponds to typically 0.2 per cent in the shear bias, so this is negligible compared to the statistical error.

Second, we consider the effect caused by a misestimation of the PSF ellipticities. One nice feature of the cluster lensing measurement is that it measures the coherent tangential shear pattern inherent in background galaxy ellipticities with respect to the cluster center, but an imperfect estimate of PSF ellipticities may not necessarily mimic the tangential shear pattern. As a possible maximum effect, assuming completely ineffective PSF correction for very poorly-resolved galaxies, we simply calculated the average of star ellipticities in each annular bin used for the shear analysis. The average ellipticity is consistent with zero in the outer radial within the standard deviation, but the average in the second and third bins deviates from zero by more than  $2\sigma$ :  $\langle g^* \rangle \simeq -0.006$ . We can estimate a maximum effect by assuming that the average PSF ellipticity propagates into the systematic error of the shear estimate, which should not be the case after the PSF correction. The bias

$\delta g_+/g_+ \simeq -0.006/0.1 \simeq -0.06$ , is  $-6$  per cent, where  $g_+ \simeq 0.1$  is the shear amplitude in the inner bins as shown in Fig. 6.

#### 4.2.4 Total budget of systematic errors on cluster mass

We can now sum up all the systematic errors in the shear estimates we have so far described. If a shear bias is negative, such that  $m < 0$  for the shear multiplicative bias, the true shear value should be higher, and in turn the true cluster mass is higher than estimated. Thus we refer to possible corrections in the cluster mass, according to the systematic errors of the cluster mass; e.g., for the multiplicative shear error of  $-6$  per cent ( $m = -0.06$ ), we refer to the correction in the cluster mass as “+7 per cent”. We found such a possible correction in the cluster mass by re-fitting the NFW profile to reduced shear which is manually corrected for the bias predicted in the previous subsections.

Summing up these possible systematic errors in quadrature, the total amount of the correction in the cluster mass is estimated as +17 per cent and  $-8$  per cent, which is about half of the statistical error in Table 3.

### 4.3 Systematic Uncertainties from Physical Considerations

In Section 4.1, we constrained the cluster mass by deprojecting two-dimensional lensing information assuming that the mass distribution of ACTJ0022 follows a spherically-symmetric NFW profile. However, dark matter halos are triaxial in general, as seen in  $\Lambda$ CDM simulations (Jing & Suto 2002). Thus the mass estimate assuming spherical symmetry can be biased. Oguri et al. (2005) estimated the halo triaxiality effect on lensing measurements, and showed that the mass can be biased by  $\pm 20 - 30$  per cent depending on the projection direction. The amount of the possible mass bias corresponds to  $\pm 50 - 70$  per cent ( $\pm 30 - 50$  per cent) of the statistical error when the concentration parameter is free (fixed).

When fitting an NFW profile to the tangential shear profile, we assumed that the BCG position (R.A.=00:22:13.04, Dec.=−00:36:33.84) is the cluster center. However, the BCG may have an offset from the true center of the dark matter halo hosting the cluster. If an off-centered BCG is assumed to be at the center of the dark matter halo profile, the tangential shear signal is diluted at radii smaller than the offset radius (Oguri & Takada 2011). By using the halo centers inferred by various observables such as X-ray and/or distribution of satellite galaxies for low-redshift clusters at  $z \sim 0.2$ , previous work showed that a typical displacement, if it exists, is about 2–3 percent of the virial radius<sup>10</sup> (van den Bosch et al. 2005; Koester et al. 2007; Bildfell et al. 2008). Assuming a similar amount of displacement for the BCG of ACTJ0022 at  $z = 0.81$ , we study how the shear signals are changed. To be more precise, we recalculated the tangential shear measurements by taking 8 different centers along the circle of radius  $0.03r_{\text{vir}}$ , with different position angles stepped by 45 degrees ( $\theta = 0, 45, \dots, 315$  degrees). Note that we employed the best-fit  $r_{\text{vir}}$  for Case 1 and 2, respectively, as given in Table 3. We found that 7 (6) out of the 8 different centers yield smaller best-fit cluster masses for Case 1 (2), respectively. Hence, a possible bias in the cluster mass due to the offset is estimated as 10 (7) per cent for Case 1 (2). This result implies that the BCG position is close to the true center. The BCG center is also supported by the high-resolution SZ observation, done by Reese

<sup>10</sup> This statement is true in the absence of photo- $z$  errors, which can cause selection of the wrong galaxy as the BCG.

et al. (2012) with SZA; the estimated center is R.A.=00:22:13.006, Dec.=−00:36:33.35 with error of  $0.8''$  and  $1.1''$ , respectively, in good agreement with the BCG position.

The mass distribution at different redshifts along the same line-of-sight of ACTJ0022 may contaminate the weak lensing signal – the so-called projection effect. The projection effect is equivalent to weak lensing due to large-scale structures (hereafter simply cosmic shear), and acts as a statistical noise to the cluster lensing. It is difficult to quantify the impact of the projection effect on individual cluster lensing, unless a prominent structure at a different redshift is identified, e.g., from a concentration of galaxies, which we do not find. Here we estimate the systematic error by assuming the typical projection effect expected for the  $\Lambda$ CDM model. We follow the method in Oguri & Takada (2011) (see discussion around Eq. 47) in order to include the covariance error matrix between the tangential shear signals of different radii due to the typical projection effect for the  $\Lambda$ CDM model. Then we re-did the  $\chi^2$ -fitting, and found that the best-fit cluster mass is changed only by about +4 per cent, which is much smaller than the statistical error due to the shape noise. The statistical error of mass estimate is increased by +3 per cent due to the covariance error matrix.

### 4.4 Cosmological Implications

#### 4.4.1 Scaling Relation

The lensing mass of ACTJ0022 can be compared with the mass estimate in Reese et al. (2012), where the two kinds of mass estimates were shown using the deep SZA observation and the SDSS Stripe 82 data (Frieman et al. 2008). First, they estimated the cluster mass from the observed Compton- $y$  parameter assuming the hydrostatic equilibrium and the universal pressure profile that is derived from the X-ray observations of 33 low-redshift clusters ( $z \lesssim 0.2$ ) in Arnaud et al. (2010). With the surface pressure correction proposed in Mroczkowski (2011), the cluster mass was estimated as  $M_{500\rho_c}^{\text{SZ}} = (0.40 \pm 0.03) \times 10^{15} M_\odot/h$ . Second, they used the scaling relation between the optical richness (the number of member galaxies) and the weak-lensing masses, done in Rozo et al. (2009) for the MaxBCG catalog (Koester et al. 2007), in order to infer the mass of ACTJ0022 assuming that the scaling relation holds for the high redshift of ACTJ0022. Then the cluster mass was derived as  $M_{500\rho_c}^{\text{N-MWL}} = (0.54 \pm 0.08) \times 10^{15} M_\odot/h$  from the inferred member galaxies of SDSS Stripe 82 data. If we re-do the cluster mass estimate from the measured tangential shear profile, assuming the cluster mass definition  $M_{500\rho_c}$  (500 times the critical density) and the same  $\Lambda$ CDM cosmology Reese et al. (2012) used ( $\Omega_m = 0.3$  and  $H_0 = 70 \text{ km s}^{-1} \text{ Mpc}^{-1}$ ), we find  $0.59_{-0.21}^{+0.23} \times 10^{15} M_\odot/h$ , which is consistent with the mass estimates in Reese et al. (2012).

In Fig. 7, we compare our lensing mass estimate for ACTJ0022 with the mass estimates of Reese et al. (2012) in the Compton- $y$  and cluster mass plane, also comparing with other results for low- $z$  clusters in Marrone et al. (2011). The Compton- $y$  parameter we quote is defined as

$$Y_{\Delta\rho_c} \equiv \frac{k_B \sigma_T}{m_e c^2} \int^{r < r_{\Delta\rho_c}} n_e(r) T_e(r) dV, \quad (29)$$

where  $T_e$ ,  $m_e$ , and  $n_e$  are temperature, mass, and density of electrons in the hot cluster gas, and  $\sigma_T$  is the cross section of Thomson scattering. Marrone et al. (2011) compared the  $y$ -parameter derived from the SZA observations with the weak lensing masses in Okabe et al. (2010) for 18 X-ray luminous clusters in the redshift range

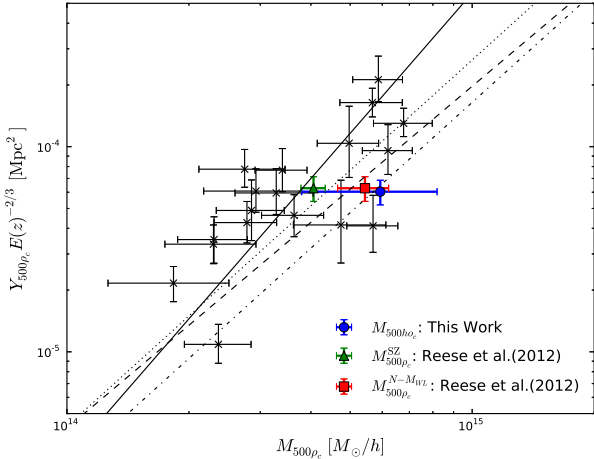


**Figure 7.** The circle symbol with error bars shows our weak lensing results for ACTJ0022 ( $z = 0.81$ ), in the plane of the Compton- $y$  parameter  $Y_{500\rho_c}$  and the cluster mass  $M_{500\rho_c}$  (for the overdensity of 500 times the critical density). Note that the  $Y_{500\rho_c}$  value quoted is taken from Reese et al. (2012) and  $E(z)$  is the redshift evolution of the Hubble expansion rate. For comparison, the triangle and square symbols (slightly shifted vertically for clarity) are taken from Reese et al. (2012), showing the mass estimates for ACTJ0022 derived using the SZA observation with the virial theorem and the optical-richness and mass scaling relation of the SDSS clusters, respectively. The star symbols are from Marrone et al. (2011), derived using the SZA observations and the weak lensing mass estimates for the 18 LoCuSS clusters at redshift  $z \simeq 0.2$ . The solid line denotes the best-fit scaling relation. The dashed line denotes the scaling relation in Andersson et al. (2011) for the SPT SZ clusters in the wide redshift range up to  $z \sim 1$ , which is derived combining the SZ observation with the X-ray follow-up observations. The dotted line denotes the scaling relation in Arnaud et al. (2010), derived using the X-ray observations for low-redshift clusters at  $z \lesssim 0.2$ . The dot-dashed line denotes the scaling relation in Sifón et al. (2012), derived using the dynamical mass estimates for the ACT SZ clusters in the wide redshift range up to  $z \sim 1$ .

$z = [0.15, 0.3]$ , which are in the LoCuSS sample<sup>11</sup>. Then they derived the scaling relation assuming the power-law form, denoted by the solid line. Our weak lensing mass of ACTJ0022 seems to prefer a higher mass for a fixed  $Y_{\Delta\rho_c}$  than the scaling relation, but again not significant due to the large error bars. The dotted and dashed lines show the scaling relations derived in Arnaud et al. (2010) and Andersson et al. (2011), which are based on the X-ray observations for low- $z$  clusters ( $z \lesssim 0.2$ ) and the SPT SZ clusters, respectively. In particular, Andersson et al. (2011) made the follow-up Chandra and XMM-Newton observations of the 15 SPT-selected clusters, which cover a wide range of redshifts up to  $z = 1$  and has the mean redshift of 0.67. The dot-dashed line shows the scaling relations derived in Sifón et al. (2012), which is based on the dynamical mass estimates for the ACT SZ clusters ranging from  $z = 0.28$  to  $z = 1.06$  with the mean redshift of 0.55. Our weak lensing mass of ACTJ0022, which is also a high- $z$  SZ cluster, seems to lie closer to the scaling relation of Andersson et al. (2011) and Sifón et al. (2012), but more observations are definitely needed to derive a more robust conclusion.

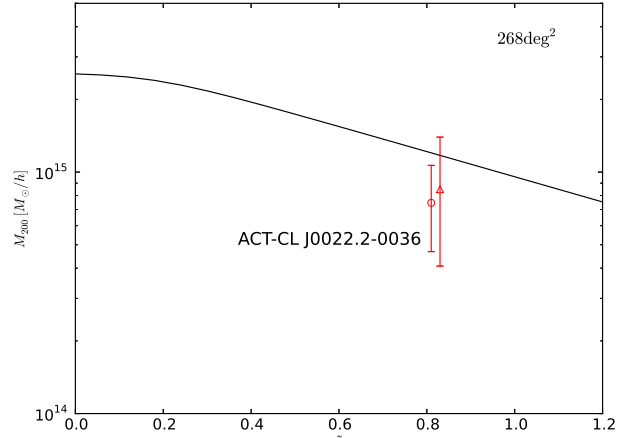


**Figure 8.**  $\Lambda$ CDM-model derived exclusion curve with 95% C.L. for cluster mass of the most massive cluster in a survey area of 268 square degrees, close to the ACT survey area, which is computed based on the method in Mortonson et al. (2011). If any cluster is found to have its mass above the curve, it gives conflict with the  $\Lambda$ CDM model that is consistent with other various observations. The circle and diamond points (slightly shifted horizontally for clarity) denote our weak lensing mass estimates for ACTJ0022 (see Table 3), and the error bars show  $1\sigma$  statistical error.

#### 4.4.2 $\Lambda$ CDM Exclusion Curve

ACTJ0022 is one of the most luminous SZ clusters at high redshift. The existence of massive and higher redshift clusters gives a stringent test of the  $\Lambda$ CDM structure formation model as well as the nature of the primordial perturbations. Here we use the method in Mortonson et al. (2011) to address whether or not the existence of ACTJ0022 is consistent with the  $\Lambda$ CDM prediction. To make the test, we use the weak lensing mass estimate rather than the X-ray or SZ-derived masses.

Fig. 8 shows the result. The solid curve shows the 95% C.L. confidence level curve, computed using the code publicly available from the website<sup>12</sup> (Mortonson et al. 2011); if any cluster lying above the curve were found, it could falsify or at least challenge the standard  $\Lambda$ CDM model that is constrained by observations such as CMB, SNe, and BAO. To compute the confidence curve, we assumed 268 square degrees for the ACT survey region overlapping with SDSS Stripe 82. The circle and triangle symbols are the mass estimates for Case 1 and 2 in Table 3, which are both under the exclusion curve. Hence the existence of ACTJ0022 is consistent with the  $\Lambda$ CDM model. Note that Eddington bias is not corrected in Fig. 8. However, since the mass function steeply falls with mass, the mass is reduced after the correction. Thus, the conclusion we made above does not change.

## 5 CONCLUSIONS

In this paper, we have used multi-band ( $Br'i'z'Y$ ) Subaru images to study the weak lensing signal for ACTJ0022 at  $z = 0.81$ , which is one of the most luminous SZ clusters identified by the ACT survey. By using photometric redshifts derived from the multi-band

<sup>11</sup> <http://www.sr.bham.ac.uk/locuss/>

<sup>12</sup> <http://background.uchicago.edu/abundance/>

data, we built a robust catalog of background galaxies behind the high-redshift cluster, leaving us a lower number of background galaxies,  $3.2 \text{ arcmin}^{-2}$  compared to the original density of about  $20 \text{ arcmin}^{-2}$  for all the galaxies usable for weak lensing analysis. Nevertheless, we detected the lensing distortion signal at  $3.7\sigma$ , suggesting that the SZ-luminous ACTJ0022 is a massive cluster with virial mass  $M_{200} \sim 0.8 \times 10^{15} M_{\odot}/h$  (see Fig. 6 and Table 3).

While the statistical significance of this detection is not high, we nonetheless were careful in how we did the weak lensing analysis. First, we developed a method of using different exposure images to model the shape of each galaxy image. In this simultaneous multi-exposure fitting method, we can use the same model parameters for each galaxy over the different exposures, and can use the PSFs from each exposure, which allows us to keep the highest-resolution images and avoid a mixture of different PSFs. Note that we did use the stacked image for object detection. Due to the gain in the spatial resolution, we can use slightly smaller-size galaxies for the lensing shape measurement, by about 10 per cent, compared to the analysis using the stacked image, where each galaxy image is more affected by the PSF smearing effect, especially the worst-seeing exposure. We also developed a diagnostic method of using the star-galaxy correlation *residual* function, in order to identify particular exposures that may cause systematic error in the shape measurement (see Section 3.4.4 and Fig. 5). Secondly, in the PSF and galaxy shape measurements, we included astrometric, optical distortion effect by fitting the star and galaxy images in the celestial coordinates. The astrometric distortion is treated as a coordinate transformation between the CCD pixel coordinates and the celestial coordinates, not a convolution effect as for the PSF smearing. We believe that these methods can potentially improve our ability to accurately measure the PSF and galaxy shapes, by minimizing systematic errors, which are desired for upcoming wide-area weak lensing surveys such as the Subaru HSC survey and DES.

Our method of estimating galaxy photometry for photo- $z$  was also designed to minimize systematic error. Following the method in Hildebrandt et al. (2012), we measured the color of every galaxy in the *same* physical region. To do this, we made a PSF matching/homogenization for the stacked images of different passbands in order to have the same PSFs in different passbands and across different positions in each image (see Table 2). Then, by defining the same aperture region around each galaxy which is defined in the WCS, we could measure the color of the galaxy in the same region. We tested our photo- $z$  estimate by comparing with the spectroscopic redshifts of cluster members taken with Gemini/GMOS, which shows a good agreement with our photo- $z$  estimates (see Fig. 3). However, since we also found photo- $z$  outlier contamination at  $z_p > 2$ , we imposed a rather stringent cut on the photo- $z$ ,  $0.95 < z < 2.0$  to define a secure catalog of background galaxies used for our lensing analysis. For the data reduction/image processing, we used tools from the pipeline being developed for the HSC survey.

Our lensing mass estimates for ACTJ0022,  $M_{200} = 0.75_{-0.28}^{+0.32} \times 10^{15} M_{\odot}/h$  ( $M_{200} = 0.85_{-0.44}^{+0.55} \times 10^{15} M_{\odot}/h$ ) for the NFW fitting with a free (fixed to 4.0) concentration parameter, are consistent with the mass estimates from the SZA observations assuming hydrostatic equilibrium and from the optical richness-WL mass scaling relation in Reese et al. (2012), within the statistical measurement errors (Fig. 7). We also discussed what the mass estimate for the high- $z$  SZ cluster ACTJ0022 may imply for the scaling relation of the Compton- $y$  and cluster mass, comparing with the scaling relations studied in previous works (Andersson et al. 2011; Arnaud et al. 2010; Marrone et al. 2011). The cluster observable

and mass scaling relation is of critical importance for cluster cosmology (Weinberg et al. 2012). Our study is the first step towards building the SZ and WL mass scaling relation for high- $z$  clusters, and we must increase the size of the sample of high-redshift SZ clusters to study their WL signals. Joint optical and SZ experiments will be increasingly important for the upcoming surveys, the Subaru HSC survey and the DES, which overlap the ACT and SPT SZ surveys.

Our result demonstrates the difficulty in obtaining a high signal-to-noise ratio WL measurements for individual high- $z$  clusters, due to the small number density of background galaxies and photo- $z$  limitations. In addition, there are physical effects that cause systematic issues for the WL mass estimate of individual clusters; projection effects and aspherical mass distributions that are unavoidable even for a perfect WL measurement. To overcome these obstacles, we can use stacked lensing measurement or cluster-shear correlation function method in order to boost the WL signal-to-noise ratios and remove the systematic errors after the statistical average (Oguri & Takada 2011; Mandelbaum et al. 2012). For upcoming surveys such as the HSC, we can expect to find over a thousand massive clusters with  $\geq 10^{14} M_{\odot}$  at  $z > 1$  over 1500 square degrees. Such a stacking analysis will be powerful to obtain the average cluster mass as well as study the scaling relations of the WL mass and cluster observables as a function of the binned cluster observables (Fang et al. 2012). The stacked lensing is based on a careful WL analysis of individual cluster regions, but the increased  $S/N$  coming from the stack makes us more sensitive to systematic errors; thus, the methods we developed in this paper will be useful for upcoming surveys.

## ACKNOWLEDGMENTS

H.M. and M.T. greatly thank Gary Bernstein, Bhuvnesh Jain and Mike Jarvis for many useful and constructive discussion on the shape measurement methods. H.M. acknowledges support by MEXT/JSPS Grant-in-Aid for JSPS Fellows (DC1). This work is supported in part by JSPS KAKENHI (Grant Number: 23340061), JSPS Core-to-Core Program “International Research Network for Dark Energy”, by World Premier International Research Center Initiative (WPI Initiative), MEXT, Japan, and by the FIRST program “Subaru Measurements of Images and Redshifts (SuMIRE)”, CSTP, Japan.

This work is based in part on data collected at Subaru Telescope, which is operated by the National Astronomical Observatory of Japan.

Funding for SDSS-III has been provided by the Alfred P. Sloan Foundation, the Participating Institutions, the National Science Foundation, and the U.S. Department of Energy Office of Science. The SDSS-III web site is <http://www.sdss3.org/>.

SDSS-III is managed by the Astrophysical Research Consortium for the Participating Institutions of the SDSS-III Collaboration including the University of Arizona, the Brazilian Participation Group, Brookhaven National Laboratory, University of Cambridge, Carnegie Mellon University, University of Florida, the French Participation Group, the German Participation Group, Harvard University, the Instituto de Astrofísica de Canarias, the Michigan State/Notre Dame/JINA Participation Group, Johns Hopkins University, Lawrence Berkeley National Laboratory, Max Planck Institute for Astrophysics, Max Planck Institute for Extraterrestrial Physics, New Mexico State University, New York University, Ohio State University, Pennsylvania State University, University of



Portsmouth, Princeton University, the Spanish Participation Group, University of Tokyo, University of Utah, Vanderbilt University, University of Virginia, University of Washington, and Yale University.

## REFERENCES

- Aihara H. et al., 2011, *ApJS*, 193, 29  
 Alard C., 2000, *A&AS*, 144, 363  
 Alard C., Lupton R. H., 1998, *ApJ*, 503, 325  
 Andersson K. et al., 2011, *ApJ*, 738, 48  
 Arnaud M., Pratt G. W., Piffaretti R., Böhringer H., Croston J. H., Pointecouteau E., 2010, *A&A*, 517, A92  
 Arnouts S., Cristiani S., Moscardini L., Matarrese S., Lucchin F., Fontana A., Giallongo E., 1999, *MNRAS*, 310, 540  
 Bartelmann M., 1996, *A&A*, 313, 697  
 Bartelmann M., Schneider P., 2001, *Phys. Rep.*, 340, 291  
 Bernstein G. M., Jarvis M., 2002, *AJ*, 123, 583  
 Bertin E., Arnouts S., 1996, *A&AS*, 117, 393  
 Bildfell C., Hoekstra H., Babul A., Mahdavi A., 2008, *MNRAS*, 389, 1637  
 Bolton A. S. et al., 2012, *ArXiv e-prints*  
 Broadhurst T., Takada M., Umetsu K., Kong X., Arimoto N., Chiba M., Futamase T., 2005, *ApJ Lett.*, 619, L143  
 Carlstrom J. E. et al., 2011, *PASP*, 123, 568  
 Carlstrom J. E., Holder G. P., Reese E. D., 2002, *ARA&A*, 40, 643  
 Castelli F., Kurucz R. L., 2004, *ArXiv Astrophysics e-prints*  
 Coleman G. D., Wu C.-C., Weedman D. W., 1980, *ApJS*, 43, 393  
 Dawson K. S. et al., 2012, *ArXiv e-prints*  
 Duffy A. R., Schaye J., Kay S. T., Dalla Vecchia C., 2008, *MNRAS*, 390, L64  
 Eisenstein D. J. et al., 2011, *AJ*, 142, 72  
 Fang W., Kadota K., Takada M., 2012, *Phys. Rev. D*, 85, 023007  
 Frieman J. A. et al., 2008, *AJ*, 135, 338  
 Hasselfield, in prep.  
 Hildebrandt H. et al., 2012, *MNRAS*, 2386  
 Hirata C. M. et al., 2004, *MNRAS*, 353, 529  
 Huff E. M., Hirata C. M., Mandelbaum R., Schlegel D., Seljak U., Lupton R. H., 2011, *ArXiv e-prints*  
 Ilbert O. et al., 2006, *A&A*, 457, 841  
 Ilbert O. et al., 2009, *ApJ*, 690, 1236  
 Iye M. et al., 2004, *PASJ*, 56, 381  
 Jing Y. P., Suto Y., 2002, *ApJ*, 574, 538  
 Jolliffe I. T., 1986, *Principal component analysis*, Jolliffe, I. T., ed.  
 Kinney A. L., Calzetti D., Bohlin R. C., McQuade K., Storchi-Bergmann T., Schmitt H. R., 1996, *ApJ*, 467, 38  
 Kitayama T., Suto Y., 1997, *ApJ*, 490, 557  
 Koester B. P. et al., 2007, *ApJ*, 660, 239  
 Lang D., Hogg D. W., Mierle K., Blanton M., Roweis S., 2010, *AJ*, 139, 1782  
 Lupton R., Gunn J. E., Ivezić Z., Knapp G. R., Kent S., Yasuda N., 2001, in *Astronomical Society of the Pacific Conference Series*, Vol. 238, *Astronomical Data Analysis Software and Systems X*, F. R. Harnden Jr., F. A. Primini, & H. E. Payne, ed., p. 269  
 Mandelbaum R., Slosar A., Baldauf T., Seljak U., Hirata C. M., Nakajima R., Reyes R., Smith R. E., 2012, *ArXiv e-prints*  
 Marriage T. A. et al., 2011, *ApJ*, 731, 100  
 Marrone D. P. et al., 2011, *ArXiv e-prints*  
 Menanteau, in prep.  
 Miyatake H., in prep.  
 Miyazaki S. et al., 2002a, *ApJ Lett.*, 580, L97  
 Miyazaki S. et al., 2006, in *Society of Photo-Optical Instrumentation Engineers (SPIE) Conference Series*, Vol. 6269, *Society of Photo-Optical Instrumentation Engineers (SPIE) Conference Series*  
 Miyazaki S. et al., 2002b, *PASJ*, 54, 833  
 Mortonson M. J., Hu W., Huterer D., 2011, *Phys. Rev. D*, 83, 023015  
 Mroczkowski T., 2011, *ApJ Lett.*, 728, L35  
 Nakajima R., Bernstein G., 2007, *AJ*, 133, 1763  
 Navarro J. F., Frenk C. S., White S. D. M., 1996, *ApJ*, 462, 563  
 Nishizawa A. J., Takada M., Hamana T., Furusawa H., 2010, *ApJ*, 718, 1252  
 Oguri M., Bayliss M. B., Dahle H., Sharon K., Gladders M. D., Natarajan P., Hennawi J. F., Koester B. P., 2012, *MNRAS*, 420, 3213  
 Oguri M., Takada M., 2011, *Phys. Rev. D*, 83, 023008  
 Oguri M., Takada M., Umetsu K., Broadhurst T., 2005, *ApJ*, 632, 841  
 Okabe N., Takada M., Umetsu K., Futamase T., Smith G. P., 2010, *PASJ*, 62, 811  
 Reese E. D. et al., 2012, *ApJ*, 751, 12  
 Reichardt C. L. et al., 2012, *ArXiv e-prints*  
 Rozo E. et al., 2009, *ApJ*, 699, 768  
 Schlegel D. J., Finkbeiner D. P., Davis M., 1998, *ApJ*, 500, 525  
 Sehgal N. et al., 2011, *ApJ*, 732, 44  
 Shupe D. L., Moshir M., Li J., Makovoz D., Narron R., Hook R. N., 2005, in *Astronomical Society of the Pacific Conference Series*, Vol. 347, *Astronomical Data Analysis Software and Systems XIV*, Shopbell P., Britton M., Ebert R., eds., p. 491  
 Sifón C. et al., 2012, *ArXiv e-prints*  
 Smee S. et al., 2012, *ArXiv e-prints*  
 Sunyaev R. A., Zeldovich Y. B., 1972, *Comments on Astrophysics and Space Physics*, 4, 173  
 Swetz D. S. et al., 2011, *ApJS*, 194, 41  
 The Dark Energy Survey Collaboration, 2005, *ArXiv Astrophysics e-prints*  
 van den Bosch F. C., Weinmann S. M., Yang X., Mo H. J., Li C., Jing Y. P., 2005, *MNRAS*, 361, 1203  
 Vanderlinde K. et al., 2010, *ApJ*, 722, 1180  
 Vikhlinin A. et al., 2009, *ApJ*, 692, 1060  
 Weinberg D. H., Mortonson M. J., Eisenstein D. J., Hirata C., Riess A. G., Rozo E., 2012, *ArXiv e-prints*  
 Wright C. O., Brainerd T. G., 2000, *ApJ*, 534, 34  
 Zeldovich Y. B., Sunyaev R. A., 1969, *Ap&SS*, 4, 301